Numerical Studies of Flow and Associated Losses in the Exhaust Port of a Diesel Engine

by

Yue Wang

November 2013
Technical Reports from
Royal Institute of Technology
KTH Mechanics
SE-100 44 Stockholm, Sweden

Akademisk avhandling som med tillstånd av Kungliga Tekniska Högskolan i Stockholm framlägges till offentlig granskning för avläggande av teknologie doktorsexamen Tisdagen den 17/12 2013 kl 10:00 i sal F3, Lindstedtsvägen 26, Kungliga Tekniska Högskolan, Vallhallavägen 79, Stockholm.

©Yue Wang 2013
Universitetsservice US–AB, Stockholm 2013

Numerical Studies of Flow and Associated Losses in the Exhaust Port of a Diesel Engine

Yue Wang 2013,
KTH Mechanics
SE-100 44 Stockholm, Sweden

Abstract

In the last decades, the focus of internal combustion engine development has moved towards more efficient and less pollutant engines. In a Diesel engine, approximately 30-40% of the energy provided by combustion is lost through the exhaust gases. The exhaust gases are hot and therefore rich of energy. Some of this energy can be recovered by recycling the exhaust gases into turbocharger. However, the energy losses in the exhaust port are highly undesired and the mechanisms driving the total pressure losses in the exhaust manifold not fully understood. Moreover, the efficiency of the turbine is highly dependent on the upstream flow conditions.

Thus, a numerical study of the flow in the exhaust port geometry of a Scania heavy-duty Diesel engine is carried out mainly by using the Large Eddy Simulation (LES) approach. The purpose is to characterize the flow in the exhaust port , analyze and identify the sources of the total pressure losses. Unsteady Reynolds Averaged Navier-Stokes (URANS) simulation results are included for comparison purposes. The calculations are performed with fixed valve and stationary boundary conditions for which experimental data are available. The simulations include a verification study of the solver using different grid resolutions and different valve lift states. The calculated numerical data are compared to existent measured pressure loss data. The results show that even global parameters like total pressure losses are predicted better by LES than by URANS. The complex three-dimensional flow structures generated in the flow field are qualitatively assessed through visualization and analyzed by statistical means. The near valve region is a major source of losses. Due to the presence of the valve, an annular, jet-like flow structure is formed where the high-velocity flow follows the valve stem into the port. Flow separation occurs immediately downstream of the valve seat on the walls of the port and also on the surface of the valve body. Strong longitudinal, non-stationary secondary flow structures (i.e. in the plane normal to the main flow direction) are observed in the exhaust manifold. Such structures can degrade the efficiency of a possible turbine of a turbocharger located downstream on the exhaust manifold.

The effect of the valve and piston motion has also been studied by the Large Eddy Simulation (LES) approach. Within the exhaust process, the valves open while the piston continues moving in the combustion chamber. This

process is often analyzed modeling the piston and valves at fixed locations, but conserving the total mass flow. Using advanced methods, this process can be simulated numerically in a more accurate manner. Based on LES data, the discharge coefficients are calculated following the strict definition. The results show that the discharge coefficient can be overestimated (about 20 %) when using simplified experiments, e. g. flow bench. Simple cases using fixed positions for valve and piston are contrasted with cases which consider the motion of piston and/or valves. The overall flow characteristics are compared within the cases. The comparison shows it is impossible to rebuild the dynamic flow field with the simplification with fixed valves. It is better to employ LES to simulate the dynamic flow and associated losses with valve and piston motion.

Descriptors: Internal Combustion Engine, Exhaust flow, Exhaust Valve, Exhaust Port, Large Eddy Simulation, Valve and Piston Motion, Total Pressure Losses, Energy Losses, Discharge coefficient, Flow Losses, Flow structures, Air Flow Bench, Engine-like Conditions.

Numerisk studie av flödet och de associerade förlusterna i avgasporten hos en dieselmotor

Yue Wang 2013,
KTH Mechanik
SE-100 44 Stockholm, Sverige

Sammanfattning

Under de senaste decennierna såhar utvecklingsfokus av förbränningsmotorer flyttats mot mer effektiva motorer som även ger mindre utsläpp. I en dieselmotor såförsvinner ca 30-40% av den tillförda energin ut med avgaserna, dessa avgaser har hög temperatur och är därför energirika. En del av denna energi kan tas till vara pågenom att använda en turboladdare. Dock såär energiförlusterna i avgasporten icke önskvärda och de mekanismer som styr total tryckfallet är inte helt kända. Dessutom såär turbinverkningsgraden starkt beroende påhur strömningsfältet ser ut uppströms.

Detta medför att en numerisk studie av flödet igenom en avgasport tillhörande en Scania lastbilsdieselmotor har utförts, huvudsakligen genom att använda Large Eddy Simuleringar (LES). Syftet är att karaktärisera flödet genom avgasporten, samt att analysera och identifiera källorna till totaltryckförlusten. Resultat från Unsteady Reynolds Averaged Navier -Stokes (URANS) simuleringar har lagts till av jämförelseskäl. Beräkningarna är gjorda vid fasta ventillyft och stationära randvillkor, dåexperimentell data finns tillgänglig. Simuleringarna inkluderar en verifieringsstudie av lösaren genom att använda olika nätupplösningar och olika ventillyft. De beräknade resultaten jämförs med tryckförlustresultaten från experimenten. Resultaten visar att även globala parameterar såsom totaltryckförlusten predikteras bättre med LES än utav URANS. De komplexa tre-dimensionella strukturerna som genereras i flödesfältet är kvalitativt bedömda utifrån visualiseringar och analyserade med hjälp av statistiska metoder. Området nära ventilen är en stor källa till förluster. Pågrund av ventilens närvaro sågenereras det en ringformad jet-liknande struktur där flöde med hög hastighet följer ventilstammen in i avgasporten. Flödesseparation uppkommer omedelbart nedströms ventilsätet påväggen i porten samt påytan av ventilkroppen. Starka longitudinella in-stationära sekundära flödesstrukturer (i planet vinkelrätt mot huvudströmningsriktningen) observeras i grenröret. Sådana strukturer kan minska turbineffektiviteten hos turboladdaren som finns nedströms efter avgasgrenröret.

Effekten av ventil och kolvrörelser har ocksåstuderats med hjälp av LES metoden. Under avgastakten såöppnas avgasventilerna under tiden som kolven rör sig i cylindern. Denna process analyseras ofta med både ventil och kolv modellerade i fast position, men med det totala massflödet bevarat. Med

hjälp av avancerade metoder såkan man simulera denna process påett mer noggrant sätt. Med hjälp av Large Eddy Simuleringsdata såräknas Utsläppskoefficient ut enligt den strikta definitionen. Resultaten visar att Utsläppskoefficient över predikteras (ca 20%) när man använder sig utan enkla experiment, t.ex. flödesbänkar. Enkla fall där ventil och kolv har fasta positioner jämförs med fall dåkolven och/eller ventilerna rör sig. Den övergripande flödeskaraktären jämförs mellan fallen. Jämförelsen visar att det är omöjligt att återskapa det dynamiska flödesfältet såventilerna är fasta. Det är bättre att använda LES för att simulera det dynamiska flödet och de associerade förlusterna med hjälp av rörlig kolv och ventiler.

Preface

This thesis is a review of my research on the exhaust flow of an Internal Combustion Engine. I feel very lucky to have such a research project which has a close relation with practice in the automotive industry. This thesis consist of two parts. The first part gives an overview of the background and motivation, turbulence modeling, computational methods and a short summary of the results. The second part consists of five papers which contained the results during the research process.

November 2013, Stockholm
Yue Wang

Contents

Abstract iii

Sammanfattning v

Preface vii

Chapter 1. Introduction 1

Chapter 2. Exhaust Flow in Internal Combustion Engines 7
2.1. Internal combustion engines 7
2.2. Flow through the exhaust port 9
2.3. Utilization of exhaust gas energy 20

Chapter 3. Turbulence and Turbulence Modeling 24
3.1. Turbulence 24
3.2. Direct Numerical Simulations, DNS 27
3.3. Turbulence modeling 27

Chapter 4. Numerical Methods for Exhaust Flow Modeling 33
4.1. Temporal discretization 35
4.2. Spatial discretization 35
4.3. Boundary conditions 36
4.4. Solution procedures 37

Chapter 5. Solver Verification and Computational Cases 38
5.1. Geometry 38
5.2. Simulated configurations 39

Chapter 6. Results and Discussion 51
6.1. "Laboratory-like condition" results 52
6.2. "Engine-like condition" results 60

Chapter 7. Summary and Future Work 68
7.1. "Laboratory-like condition" simulations 68
7.2. "Engine-like condition" simulations 69
7.3. Proposed future work 70

Chapter 8. Papers Summary and Authors Contributions 71

Acknowledgments 75

Bibliography 77

Part II 83

Paper 1: LES of the Exhaust Flow in a Heavy-Duty Engine

Paper 2: Flow Structures and Losses in the Exhaust Port of an Internal Combustion Engine

Paper 3: Flow-structures Generated by Valve and Piston Motion in an Exhaust Port of a Truck Engine

Paper 4: Flow Losses under Laboratory-like and Engine-like Conditions in the Exhaust Port of a Diesel Engine

Paper 5: Assessing Energy Losses Associated with the Pulsating Flow in the Exhaust Port of an Internal Combustion Engine

Part I

Overview and summary

CHAPTER 1

Introduction

Understanding the gas exchange process and the driven mechanisms responsible for the losses in the exhaust port of an Internal Combustion Engine (ICE) is essential in order to construct more efficient and less pollutant engines.

In vehicles, because of the space limitation, the internal combustion engine and its associated manifolds cannot be built as large as the gas efficiency will require. Actually, given the whole fuel energy released in a typical internal combustion engine, only 20-30% of the energy is used for the effective work, roughly 30-40% of the energy is lost after combustion through the exhaust gas, see e.g. Baines (2005). Some of the energy in the exhausted gas-charge can be recycled by turbocharging. Using a turbocharger one can improve roughly 5-15% of the energy to the effective work (Fu *et al.* (2013)).

The exhaust gases carry the energy through the exhaust port and manifold towards the turbine of the turbocharger system. The hot exhaust gases expand through the turbine wheel and give the energy for turbine to rotate. Thus, the turbocharger's compressor on the intake manifold is driven by the turbine via the turbocharger shaft. The compressor wheel compresses the inlet air into the intake manifold. As a result, the air density and pressure in the intake manifold increases. Thus, when the intake stroke starts, the inlet pressure does a positive work to the crankshaft. However, during the exhaust stroke, the piston needs to move against the back pressure and the back pressure does a negative work to the crankshaft.

The exhaust ports and manifold connect the engine's combustion chambers to the turbine. Energy losses in the exhaust ports and manifold occur before the interaction between the exhaust gases and the turbine blades. Such energy losses are highly undesired, affecting the performance of the turbo. The mechanisms driving the total losses in the exhaust port are not fully understood.

The exhaust flow is three dimensional (3D), highly unsteady and pulsating, it has a high temperature (up to 1000K during blow-down phase) and it may be transonic (during blow-down phase). Moreover, it is associated with a very complex geometry with valve and piston motion. The exhaust process usually begins towards the end of power stroke, 40 to 60 crank angle degrees (CAD) before bottom dead center (BDC). Once the exhaust valves open (EVO), the

pressure difference between the in-cylinder and the exhaust port region is approximately 500 kPa (5 bar), while the temperature difference is more than 300 K. Because of the high pressure difference, the gases exhaust from cylinder through the generated gap between the exhaust valve and the exhaust valve seat at a very high velocity (the flow at first is chocked). It is this phase of the exhaust process which is called the blow-down phase. After reaching BDC, the piston moves back towards the top dead center (TDC) pushing the residual gases out of cylinder. This exhaust process is normally called scavenging (or displacement) phase.

The internal combustion engine is basically a reciprocating pump and the exhaust flow is highly pulsating. However, the turbocharger is a rotary device. Here exists a matching problem between the engine and the turbocharger. Furthermore, it has been found by many researchers (Ehrlich *et al.* (1997), Piscaglia *et al.* (2007), Galindo *et al.* (2008), Hellström *et al.* (2012)), that the turbocharger efficiency is influenced, among other factors by the flow structures at the turbine inlet. Hence, the flow in the exhaust port and manifold can have a large impact on turbocharger's performance.

Unfortunately, few studies focused on a detail analysis of the flow structures in the exhausted gas-charge. Most of the experimental studies have been done on the in-cylinder flow (Crnojevic *et al.* (1999), Bensler *et al.* (2002), Towers & Towers (2004), Müller *et al.* (2010), Buschbeck *et al.* (2012) and Bücker *et al.* (2012)). The most recent ones come from Technische Universität Darmstadt (Baum *et al.* (2013*a*),Baum *et al.* (2013*b*), Peterson *et al.* (2013)). They used high-speed PIV, stereoscopic PIV and tomographic PIV to fully characterize the in-cylinder flow field in a motored optical engine. The results gave a validation data for next LES simulations. However, they did not give detailed PIV data on the flow in the intake or the exhaust ports, probably due to the limited optical access and due to the complexity of the geometry which includes parts in motion. Only single or few point measurements of static pressure and temperature data in the intake or exhaust ports are available for validating LES data. Corresponding comparisons between experiments and LES simulations have also been done by other researchers (Adomeit *et al.* (2007), Rezaei *et al.* (2010), Yu *et al.* (2006),Piscaglia *et al.* (2013)). Comparing their experimental and LES results, the LES results had generally a good agreement with the experimental results for the cylinder inflow. Firstly, the flow structures have similar shapes for the PIV and LES results. Secondly, the difference of mean velocity is less than 10 percent for the fine grids used by the above mentioned authors.

One dimensional (1D) simulation and simple experiments have been combined for assessing the exhaust flow (Onorati *et al.* (2003),Onorati *et al.* (2005)). In one dimensional simulation models (e.g. GammaTechnologiesInc. (2012)),

different components of the engine, e.g. intake pipe, inter cooler, intake manifolds and ports, exhaust manifolds and ports, exhaust pipe, Exhaust Gas Recirculation (EGR) routing, EGR cooler, turbine and compressor are represented by a large number of objects like straight pipes, pipe bends, flow splits and junctions. The basic approach is in 1D simulation models is to use the compressible Navier-Stokes equations for a straight pipe of variable cross section assuming only stream-wise (axial) variations in the velocity, density and pressure. Cross sectional area variations are accounted for, assuming rotation symmetry. Other losses, such as these generated by boundary layers, secondary flow are handled by adding a loss-factor within a given segment. Each object is discretized into many sub-volumes. One dimensional basic flow relations are solved for these sub-volumes. This means that the pressure, temperature, and flow velocity data obtained by running such simulations are assumed to be constant across any given cross section of a pipe in the system. The detailed evolution in time, the dynamics and the unsteadiness of the 3D flow and the associated structures are neglected in these 1D models. Thus, the inherent shortcoming of the 1D simulation tools is due to the need for accounting for the difference between the real flow and the model 1D flow, which is than given in for of sectional (or volumetric) losses.

Commonly, the effects of complex geometries (including here also the intake and exhaust ports of cylinder heads) on the flow are assessed by using discharge or flow coefficients. Such coefficients are obtained by performing simple experiments with fixed valve lifts at low pressure drops on Flow benches (Danov (1997)). Thus, many researchers investigated experimentally the flow through the intake or the exhaust ports of ICE for different (constant) valve lifts in order to estimate the discharge coefficients associated with the intake or exhaust ports (Johanston *et al.* (1991), Ismail *et al.* (2008), Masi *et al.* (2010), Kumar & Nagarajan (2012)). For such idealized conditions, the pressure difference is much smaller than the real engine. The dynamics of the pulsating flow has been neglected. The uneven high temperature in a real engine has been reduced to room temperature. With these assumptions, they provided data to be used for calibrating one-dimensional computational models.

Typical assumptions for the 1D calculations are: the steady-state assumption (note that 1D simulations can be run also under transient conditions (Onorati *et al.* (2002))), one-dimensional flow, geometry effects are neglected, no turbulence modeling, heat transfer model assumptions. Thus, the accuracy of the predictions (e.g. the total pressure losses in the exhaust port) is restricted by these assumptions and simplifications. Moreover, one dimensional simulations cannot capture the dynamics of the 3D flow structures related to the exhaust process or their interaction with the complex geometry. Note also that important flow features like flow separation, flow structure formation, and

secondary flow motion (i.e. processes which could be major sources for energy losses) and their effects on the flow are not considered neither with 1D calculations.

Using advanced computational approaches (but much more expensive) one can capture in a more accurate manner and possible under more realistic conditions (e.g. with valve and piston motion) the flow structures and the total pressure losses in the exhaust port and during the exhaust process.

During the exhaust process, the characteristic Reynolds numbers are moderate, commonly on the order of 10 000 to 30 000 (Rutland (2011)). Since the computational effort associated with a 3D Direct Numerical Simulation (DNS) on complex geometries cannot be achieved for the time being, one has to use other alternatives for handling turbulence; models (such the Raynold Averegaed Navier-Stoles, RANS, framework) or approximations with/without explicit modeling, such as Large Eddy Simulations (LES). Three dimensional simulations based on Unsteady Reynolds Averaged Navier-Stokes (URANS) formulations with the correspondent turbulence closures (usually two-equation turbulence models) are more common within the context of internal combustion engines both in industry and in the academic world (Tahry & H. (1983), Han & Reitz (1995), Kurniawan *et al.* (2007)). There are several different turbulence models which can be use within the RANS framework (e.g. Spalart-Allmaras, Standard $k-\epsilon$, RNG $k-\epsilon$, Realizable $k-\epsilon$, $k-\omega$). One of the obvious questions which may rise is which model can give a better prediction of the flow within the context of ICE gas exchange processes. Smits (Smits (2006)) analyze the in-cylinder flow using URANS with different turbulence models. The Realizable $k-\epsilon$ model was performing best when using a structured mesh. However, the difference between the Particle Imaging Velocimetry (PIV) data used for validation purposes and URANS results clearly existed. The results showed the skin coefficient, C_f, was overestimated by more than 10 percent. It is well known the fact that within RANS-based models all the turbulence scales are modeled, thus the dynamics of the flow are filtered out. Also, such models may have difficulties in accurately predicting highly anisotropic turbulent flows involving adverse pressure gradients, flow separation and secondary induced flow motion.

It is generally agreed that Large Eddy Simulation (LES) due to its features (e.g. more accurate; solving the most energetic structures in the flow and capturing the flow dynamics; not as expensive as DNS) it may be the preferred computational tool in future for assessing flows associated with internal combustion engines. The complexity of flow physics in ICEs requires the ability to handle and capture the large unsteady structures that contribute mostly to the losses. The flow is inherently unsteady, while the valve and piston motions should be described well. The grid resolution needed for such simulations can

be satisfied since the domain of interest is confined and is of moderate size. The large scale flow structures that are resolved by LES dominate the energy in terms of the modes describe the energy content of the flow. Only the small, subgrid-scales (SGS) which are of more homogeneous and universal character has to be modeled. Thus, LES has a much higher potential in predicting the pulsatile flow found in the exhaust port of ICEs.

Most of the LES studies performed on ICE related flows have mostly focused on the in-cylinder and intake flows. Haworth's group (Haworth (1999), Haworth & Jansen (2000)) used LES method to do cycle-to-cycle simulations on a motored engine and examine the variations in swirl, tumble, and instantaneous flow structures. The Aachen group (Rezaei *et al.* (2010)) used PIV, RANS, and LES to assess swirl homogeneity for different intake valve lift strategies in high speed Diesel engines. Researchers at Lund University (Yu *et al.* (2006), Yu *et al.* (2007), Joelsson *et al.* (2008)) used LES together with experiments to study Homogeneous Charged Compression Ignition (HCCI) combustion using Diesel fuel. However, less attention was given to the dynamic flow phenomena and to the study of the flow structures occurring in the exhaust port and manifold or to the problem of assessing the total pressure losses within this context.

The present thesis focuses on characterizing and quantifying the total pressure loses within the exhaust port of a SCANIA Diesel engine by using the LES approach. A systematic study is performed for understanding the contribution of the flow and its unsteadiness to the total pressure losses within the exhaust manifold. The impact of the valve and piston motions on the total pressure losses is evaluated.

The governing equations for a compressible flow are simulated by using a finite volume code based on an Implicit Large Eddy Simulation (ILES) approach to handle turbulence. The grid resolution is assessed to be fine enough so that the contribution of the SGS terms is small as compared to the other terms in the filtered momentum equations. This approximation is the underlying reason for the name of ILES. Several LES calculations were performed to assess the effects that the simplifications of the problem have on the output. The investigated situations can be grouped into two categories of cases: i.e. "Laboratory-like condition" and "Engine-like condition" .

In "Laboratory-like condition" simulations, the exhaust valves are fixed at certain valve lifts, respectively and the piston effect is mimicked by imposing fixed inlet mass flows. The boundary conditions are chosen to match the experimental conditions used during an investigation carried out at SCANIA using the same geometry. A grid sensitivity study was carried out to verify the numerical method and the used discretization schemes. The LES results were compared against experimental data and against URANS predictions. Mode

decomposition techniques were used to characterize the dominant flow structures in the flow field. The different mechanisms driving the total pressure losses were estimated by empirical formulas. Based on the obtained data, several ideas were proposed in order to reduce the total pressure losses in the exhaust port of the ICE.

For the "Engine-like condition" simulations, the exhaust valves and the piston are moved in some cases with a similar fashion as in the actual engine work. All the "Engine-like condition" simulations consider the temperature effect as result of the combustion process (i.e. hot flow condition). The walls are modeled as isothermal walls at different temperatures. The "Engine-like condition" simulations are divided into three sub-groups resembling different levels of simplification. In the first two sub-groups, the valves are not closed completely during their motion and only a part of the exhaust process in the internal combustion engine it is considered, from 171 CAD to 324 CAD. The minimum valve lift considered is of 3.5 mm, while the maximum valve lift is of 14 mm. In the third sub-group, the exhaust valves are fully closed at the start and at the end during their motion. The whole exhaust process from 136 CAD to 359 CAD is thus simulated.

Some of the contribution and the findings with the present study are summarized below:

1, LES calculations of the flow in the exhaust port of a Diesel engine have been performed. The results provided a better agreement with the experimental data than the URANS results.

2, It has been found that unsteady, relatively large vortical structures dominate the flow in the exhaust port.

3, The mechanisms driving the total pressure loss have been characterized. About 80% of the total pressure loss was found occurring in the near gap region of the exhaust port and it has been proved that this comes from the contraction and the enlargement process of the flow. The vortex enhanced dissipation through separation and induced secondary flow motion is the main source of the total pressure loss.

4, The impact of the valve and piston motion has been assessed by running and analyzing data obtained for several cases in a systematic and efficient manner. The results showed that the discharge coefficients obtained in Flow bench experiments for fixed valve lift conditions, with low pressure ratios are not fully valid in the actual engine works.

CHAPTER 2

Exhaust Flow in Internal Combustion Engines

This chapter gives an overview on the basic characteristics concerning the exhaust flow within internal combustion engine's environment. First, a brief introduction is presented on the fundamentals of internal combustion engines. Then, some concepts regarding the losses in manifolds are given. Thus, the effects of contraction, expansion, pipe's curvature, or flow compressibility are discussed within the context of internal combustion engine's exhaust flow and associated losses. Finally, a brief description on the turbocharging system is given, which uses the energy in the exhaust gases for improving engine's performance and efficiency. It is clear that the losses associated with the exhaust port system and manifold as well as the exhaust flow characteristics (e.g. homogeneity, dominant flow structures, turbulence levels) may have implications on the performance of the turbine and thus on engine's performance. This part of the study aims in building-up the background necessary for a better understanding of the results presented later within the thesis.

2.1. Internal combustion engines

Since Nicolaus A. Otto (1832-1891) built the first four-stroke engine in 1876, modern internal combustion engines have been used widely in transportation and power generation for over 125 years and their development never stopped. At present, the focus of development has moved towards downsizing, reducing the environmental pollution, and improving the efficiency and power.

Internal combustion engines (ICE) can be divided based on their operating principles into two main types: Otto engine and Diesel engine. The main difference between the two is given by the type of combustion occurring in the combustion chamber: premixed combustion in an Otto engine and diffusion-like combustion in a Diesel engine. Figure 2.1 presents the pressure-volume diagrams of idealized four-stroke Otto and Diesel cycles. Both of them can be broken down into a sequence of separate processes: intake, compression, combustion, expansion, and exhaust.

In an Otto cycle, process 1-2 is an isentropic compression of the air (typical compression ratios of 10) as the piston moves from bottom dead center (BDC) to top dead center (TDC). Process 2-3 is a constant-volume rapid combustion.

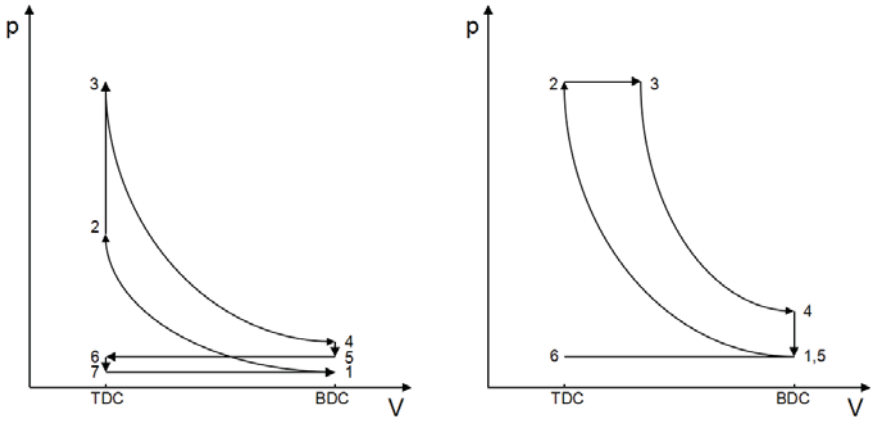

FIGURE 2.1. Left: p-V diagram of idealized throttled Otto cycle. Right: p-V diagram of idealized Diesel Cycle.

The ignition of the fuel-air mixture is caused by a spark plug. Process 3-4 is an isentropic expansion stroke while generating force and thus power. Process 4-5-6 represents the exhaust stroke. Process 6-7-1 represents the intake stroke in a throttled Otto cycle.

In an idealized Diesel cycle, air is compressed adiabatically in process 1-2 with a compression ratio typically between 1 and 2. This compression raises the temperature to the ignition temperature of the fuel mixture. Process 2-3 models a constant pressure combustion process. After that, an adiabatic expansion as a power stroke follows in process 3-4. Process 4-5-6 represents the exhaust stroke. The piston is stationary at BDC from point 4 to point 5. The cylinder pressure is above the pressure in the exhaust manifold when the exhaust valve opens at point 4. The pressure difference makes the gases escaping from the cylinder. This is known as the blow-down phase. There are two assumptions in this idealized blow-down process: the gas remaining in the cylinder expands isentropically; the gas in the manifold has the constant enthalpy after it leaves the cylinder. Following to the blow-down process (4-5), is the process 5-6 in which the piston moves from the BDC to the TDC. This is often called the scavenging pulse which pushes the burn gases out of the cylinder. Process 6-1 is the intake stroke in this idealized Diesel cycle.

For a four-stroke cycle engine, even as early as 1862, Alphonse Beau de Rochas (1815-1893) outlined the conditions which are needed in order to get the maximum efficiency:

1. The largest possible cylinder volume with the minimum boundary surface

2. The greatest possible working speed

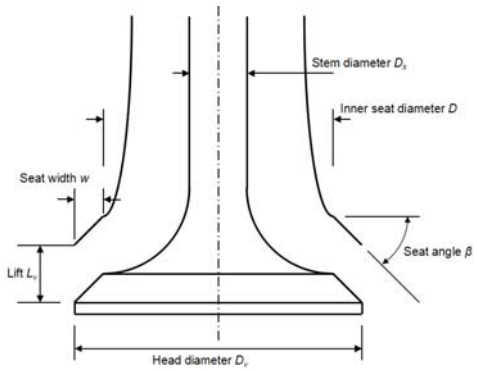

FIGURE 2.2. A typical valve and port geometry.

3. The greatest possible expansion ratio
4. The greatest possible pressure at the beginning of expansion

However, due to the space limitation of a vehicle, such an ICE cannot be build. Transforming the chemical energy contained in the fuel (by using a combustion process) into mechanical power is accompanied by a series of losses. Considering the total of energy of 100 percent resulting after the combustion process, only about 20 to 30 percent of this energy will be utilized for moving the engine's crankshaft. Among all losses (i.e. friction and parasitic losses, coolant, exhaust gas losses) the largest energy loss is through the exhaust gas.

2.2. Flow through the exhaust port

The passage formed within the valve and the exhaust port is usually the most important flow restriction in the exhaust system of any four-stroke cycle engine (Heywood (1988)).

2.2.1. *Valve and port geometry*

A typical valve and port geometry is shown in Figure 2.2. The main geometric parameters of the valve can be referenced as the diameter of the valve's head, D_v, valve stem's diameter, D_s, and valve lift, L_v. There is the valve's seat connecting the cylinder head and the exhaust port. The important parameters of the seat are the seat's width, w, seat's angle β and the inner diameter of the seat, D. The geometry of the exhaust ports often has different designs. Figure 2.3 shows the geometry design of an exhaust valve of a heavy-duty Diesel engine, i.e. SCANIA D12. The geometry is used through this thesis and is part of the computational domain (see Figure 2.3) generated for quantifying the typical exhaust flow for the SCANIA D12 engine. There are five parts in this geometry. The cylinder is marked with 1 in Figure 2.3. The piston has been

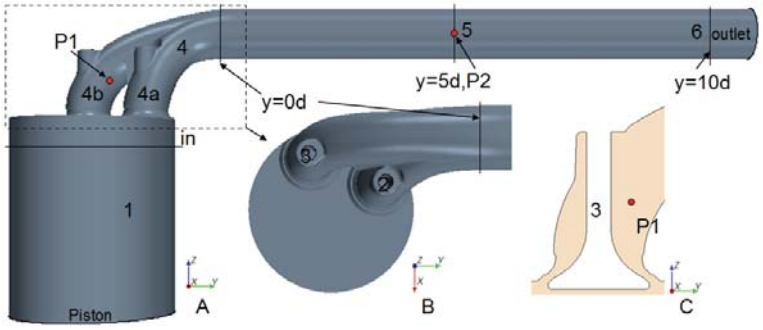

FIGURE 2.3. Details of the considered exhaust valve and ports geometries: A: The front view; B: The top view; C: Longitudinal section of valve 3. 1: Cylinder; 2 and 3: valves; 4: Exhaust port; 5: exit pipe.

simplified by not including the piston bowl. Another simplification is that the intake valves are not considered, since the intake phase is not considered here. The two exhaust valves are marked as valve numbers 2 and 3, respectively. The shapes of the exhaust valve, its seat, and exhaust port walls are visible in a section-plane passing through the centerline of valve 3 and perpendicular to the piston head, as shown in Figure 2.3C. The geometry of the exhaust port is complex with the two bend pipes (connecting the cylinder and the exit pipe) being united at one end (location y=0d in Figure 2.3). In the actual engine, the junction's end connects with the exhaust manifold. However, since only one cylinder is studied here and also to be in agreement with the experimental set-up at SCANIA (from which data were used for validation), the exhaust manifold is replaced by a long straight exit pipe.

2.2.2. *Exhaust flow field; governing equations*

The flow in the exhaust port and exhaust manifold is important for the performance of the engine within the context of making use of its energy (i.e. using a turbocharger). The flow can be characterized as being turbulent, unsteady, highly compressible, non-isothermal, transonic (in the port region), dominated by large structures downstream of the port. In summary, the complex flow poses challenges for understanding the physical details and the modeling of the flow itself. In addition, due to the complex geometry of the exhaust port and manifold, flow separation and secondary flow motion may occur.

The fluid in the exhaust flow obeys the three fundamental physical principles:

1. Mass is conserved.

2. Momentum is conserved, i.e. applying Newton's second law ($F = ma$) to fluid motion.

3. Energy is conserved.

Thus, the governing equations of the exhaust flow (Anderson (1995)) are the commonly called Navier-Stokes equations for a compressible fluid flow which describe the conservation of mass (2.1), momentum (2.2), and energy (2.3) complemented with the equation of state (2.4):

$$\frac{\partial \rho}{\partial t} + \frac{\partial (\rho u_i)}{\partial x_i} = 0 \tag{2.1}$$

$$\frac{\partial (\rho u_i)}{\partial t} + \frac{\partial (\rho u_i u_j)}{\partial x_j} = -\frac{\partial p}{\partial x_i} + \frac{\partial \sigma_{ij}}{\partial x_j} \tag{2.2}$$

$$\frac{\partial}{\partial t}(\rho(e + \frac{1}{2}u_i u_i) + \frac{\partial}{\partial x_j}(\rho u_j(h + \frac{1}{2}u_i u_i)) = \frac{\partial}{\partial x_j}(u_i \sigma_{ij}) - \frac{\partial q_j}{\partial x_j} \tag{2.3}$$

$$p = \rho R T \tag{2.4}$$

where ρ is the density, u_i, $(i = 1, 2, 3)$ is the velocity component in the i-direction, t is the time, x_i is the Cartesian coordinate in the i-direction, p is the pressure, σ_{ij} is the viscous stress tensor, e is the specific internal energy defined as $e = c_v T$, h is the specific enthalpy defined as $h = c_p T$, q_j is the heat flux can be modeled by Fourier law (2.5). The viscous shear stress tensor, σ_{ij} is defined as equation (2.6):

$$q_j = -\kappa \frac{\partial T}{\partial x_j} \tag{2.5}$$

$$\sigma_{ij} = \mu(\frac{\partial u_i}{\partial x_j} + \frac{\partial u_j}{\partial x_i} - \frac{2}{3}\delta_{ij}\frac{\partial u_k}{\partial x_k}) \tag{2.6}$$

where μ is the dynamic viscosity of the fluid. These equations, in their full form (compressible, unsteady, 3D) can be used to describe the physics of the exhaust flow. However, in many case scenarios, various assumptions on the fluid flow are made in order to simplify the problem.

2.2.3. *Bernoulli's equation and total pressure loss*

The flow in the exhaust port can be approximated as a fluid flow through a complex pipe system which includes the constriction of the valve. In such pipe line problems, Bernoulli's equation is widely used. However, Bernoullis equation assumes an incompressible, streamlined and viscous free flow. It was in 1728, when the Swiss scientist Daniel Bernoulli published his principle and stated that for an inviscid flow, an increase in the speed of the fluid occurs simultaneously with a decrease in pressure or a decrease in the fluid's potential energy. In fact, it is another statement of the energy conservation.

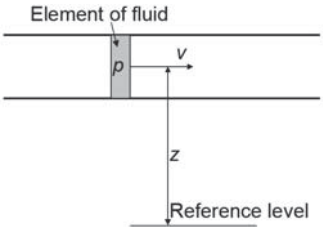

FIGURE 2.4. Element of a fluid in a pipe.

In a pipe flow problem, there are normally three forms of energy: potential energy, kinetic energy, and pressure energy. Consider an element of fluid in a pipe, as shown in Figure 2.4. Since the flow in the pipe is incompressible, the density of the fluid can be thought as constant ρ. The element of the fluid has a certain volume V, a certain velocity v and pressure p. The reference height for the pipe is z. Hence, its potential energy is $\rho V g z$, its kinetic energy is $\frac{1}{2}\rho V v^2$, and its pressure energy pV. In such a pipe system, there are no mechanical devices that would add or remove energy, no heat transferred into or out of the fluid and no energy loss due to friction. Therefore, wherever the element of the fluid moves, its energy is conserved 2.7:

$$\rho V g z + \frac{1}{2}\rho V v^2 + pV = constant \tag{2.7}$$

By dividing the volume V, equation 2.7 can be rewritten as:

$$\rho g z + \frac{1}{2}\rho v^2 + p = constant \tag{2.8}$$

The term $\frac{1}{2}\rho v^2$, in equation 2.8, is called dynamic pressure and the term p is static pressure. In many applications like for example the exhaust pipe of an ICE, the change of term $\rho g z$ is very small as compared with the other terms. Hence, the term $\rho g z$ is normally neglected and the equation 2.8 can be simplified as:

$$p_{tot} = \frac{1}{2}\rho v^2 + p = constant \tag{2.9}$$

where the total pressure p_{tot} is defined as the sum of dynamic and static pressures. Therefore, Bernoulli's principle can be summarized as total pressure is conserved everywhere in the fluid flow.In real pipe systems usually the flow is viscous and compressible, therefore energy losses occur. Thus, Bernoulli's equation is valid only approximately.

Usually, in piping systems (e.g. the exhaust manifold of an ICE) the total pressure is easily measured (e.g. by Pitot tube or manometers). Thus, the total

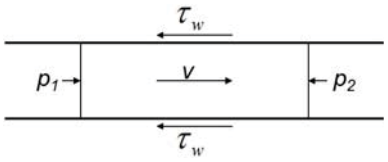

FIGURE 2.5. Forces acting on the fluid of a steady flow in a pipe.

pressure loss is normally used for judging the total energy loss in the system. Considering two sections of interest in a piping system, there is a total pressure loss Δp_{tot} between section 1 and section 2. Thus, equation 2.10 then becomes:

$$\frac{1}{2}\rho v_1^2 + p_1 = \frac{1}{2}\rho v_2^2 + p_2 + \Delta p_{tot} \tag{2.10}$$

where the total pressure loss Δp_{tot} indicates the losses associated with the flow in the pipe. The energy losses or total pressure losses can be divided into friction losses and energy losses due to obstructions.

2.2.4. *Friction losses and wall shear stress*

As the fluid moves in a pipe system, the friction always exists at the interface between the fluid and the pipe's wall. The occurring friction forces always will be opposite and resist to the fluid motion. In general, for a given pipe system, the friction F_f on the whole wall surface can be calculated by equation 2.11

$$F_f = \iint_{A_{wall}} \tau_w dA_{wall} \tag{2.11}$$

where τ_w is the wall shear stress. In experiments, the wall stress is really hard to be measured directly. The wall shear stress is due entirely to the viscous contribution (Kim *et al.* (1987). The wall shear stress can be defined, for a Newtonian fluid by:

$$\tau_w = \mu \frac{\partial u}{\partial y}|_{y=0} \tag{2.12}$$

where u is the velocity of the fluid along the boundary. The pressure drop generated by friction can be calculated in a straight pipe of a certain cross section, see Figure 2.5.

$$(p_1 - p_2)A_{eff.} = \iint_{A_{wall}} \tau_w dA_{wall} \tag{2.13}$$

where $A_{eff.}$ is the effective area of the equivalent cross section in the pipe, and $\Delta p = p_1 - p_2$ is the pressure drop generated by the friction.

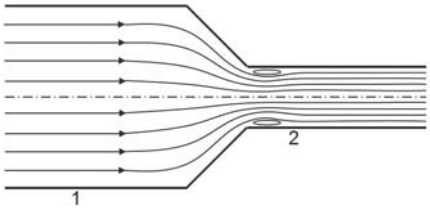

FIGURE 2.6. Flow structures in a gradual contraction.

2.2.5. *Total pressure loss due to obstructions*

Energy or total pressure losses may also occur when there are changes in the cross section of the flow path like a contraction, expansion or if there is a bend in the passage.

2.2.5a. *Contraction.* When the fluid flows through a contraction, (Figure 2.6), the velocity of the flow will increase at the site of the smallest cross-sectional area and consequently, based on Bernoulli's principle, the static pressure will decrease.

If there is no energy loss, the sum of total pressure will be conserved from location 1 to location 2. However, when the flow approaches the contraction, the flow path is curved and narrowed. At the region of the throat, the accelerated flow separates and recirculation regions are generated near by the wall at the region of minimum flow area. Eventually, the flow slightly decelerates and the path expands again to fill in the pipe 2. In a real case scenario of a turbulent flow through a contraction, energy loss occurs due to turbulence dissipation, which is also of viscous origin. This dissipation of energy means that not all the static pressure drop can be converted into kinetic energy and energy loss or total pressure loss occurs as the fluid flows through a contraction.

Energy losses are proportional to the velocity which the flow has as it moves through a contraction, expansion, or through a valve (Robert (2005)). The total pressure loss due to a contraction $\Delta p_{C_{tot}}$ can be estimated by using the following empirical relation:

$$\Delta p_{C_{tot}} = K_C \cdot \rho \frac{v_2^2}{2} \tag{2.14}$$

where v_2 is the velocity in the smaller diameter pipe 2, downstream from the contraction and K_C is the resistance coefficient. The resistance coefficient K_C has to be determined experimentally. K_C depends on the cone angle and the ratio of the diameters of the two pipes. Figure 2.7 shows the data by Idelchik (1986) for the resistance coefficient corresponding to a gradual contraction for Reynolds numbers greater than 1.0×10^5. It can be found that, at some cone

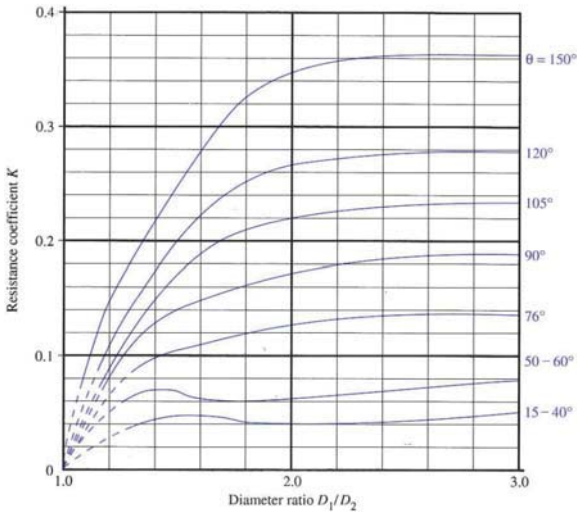

FIGURE 2.7. Resistance coefficient of gradual contraction, see Idelchik (1986).

angles, as the diameter ratio increases, the resistance coefficient due to contraction becomes constant. For example, at the 90° cone angle, the resistance coefficient is about 0.19 when the diameter ratio exceeds 2.8.

2.2.5b. *Expansion.* As the fluid flows from a smaller pipe diameter into a larger pipe through an expansion, (Figure 2.8), the velocity of the flow decreases as the pressure rises. Just downstream of the sudden expansion, recirculation regions develop. Naturally, energy losses are associated with such recirculation regions. In a similar fashion as shown for the contraction case, the energy loss due to expansion is proportional to the velocity of the flow. Therefore, the total pressure loss can be estimated by:

$$\Delta p_{E_{tot}} = K_E \cdot \rho \frac{v_1^2}{2} \tag{2.15}$$

where v_1 is the upstream velocity of the flow in the smaller pipe ahead of the expansion and K_E is the resistance coefficient due to expansion. The resistance coefficients also depends on the cone angle θ and the diameter ratio D_2/D_1. Empirical data regarding the resistance coefficient for a gradual expansion is given in Figure 2.9 (Idelchik (1986)).

2.2.5c. *The bended pipe geometry.* In addition to contractions and expansions the exhaust piping system includes also bends. As the fluid flows through a pipe bend, Figure 2.10, there is a radial pressure gradient generated by the

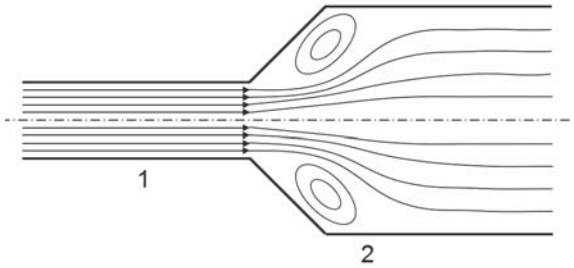

FIGURE 2.8. Flow structures in a gradual expansion.

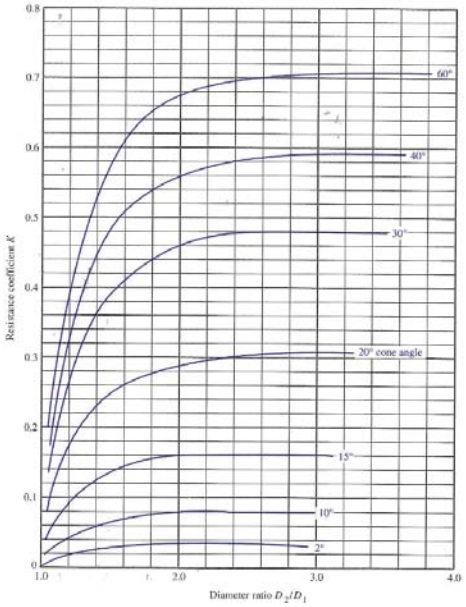

FIGURE 2.9. Resistance coefficient of gradual expansion, Idelchik (1986).

centrifugal force acting on the fluid. Due to this, the fluid in the center of the pipe is swept towards the outer side and comes back along the wall towards the inner side. This generates counter-rotating vortical structures downstream of the bend, which are known as Dean vortices(Dean (1928), Rutten *et al.* (2005),Kalpakli *et al.* (2012)).

The total pressure losses in a pipe bend can be divided into wall friction loss and total pressure loss due to momentum exchanges in the direction of the flow. The friction loss has been discussed in Section 2.2.4. The total pressure

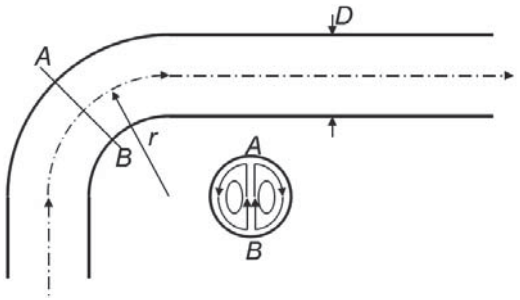

FIGURE 2.10. 90° pipe bend.

loss due to the flow through the bend and it is due to the induced secondary flow which is proportional to the velocity of the flow. An empirical relation similar to the previous cases can be formulated, using a bend loss coefficient, k_b which is given by:

$$\Delta p_{B_{tot}} = k_b \cdot \rho \frac{v^2}{2} \tag{2.16}$$

where v is the mean flow velocity (based on the bulk flow rate), while the bend loss coefficient k_b depends on the bend angle and curvature ratio. The curvature ratio is defined as the ratio between the centerline radius r of the bend and the internal diameter D of the pipe. The bend loss coefficient k_b curves as a function of the curvature ratio of the bend is depicted in Figure 2.11 (Kitto & Stultz (1978)).

2.2.6. *Compressibility of exhaust flow*

As it has been emphasized in Section 2.2.3, the Bernoulli's equation is only valid for incompressible flows, or compressible flows at low Mach numbers (bellow about 0.3). However, during engine working conditions, the exhaust flow can become transonic or supersonic. The compressibility of the exhaust flow may have significant impact on the flow behavior and flow losses.

For gases, with the flow Mach number larger than 0.3, the density changes are too large to be ignored. Normally, compressible flow can be divided into four regimes: subsonic flow with Mach number from 0.3 to 0.8; transonic flow with Mach number from 0.8 to 1.2; supersonic flow with Mach number from 1.2 to about 4 and Hypersonic flow with Mach number larger than about 4. Each of these regimes has its own physical characteristics.

In the study of compressible flows, the relation between pressure, density, and temperature for an isentropic process is frequently used.

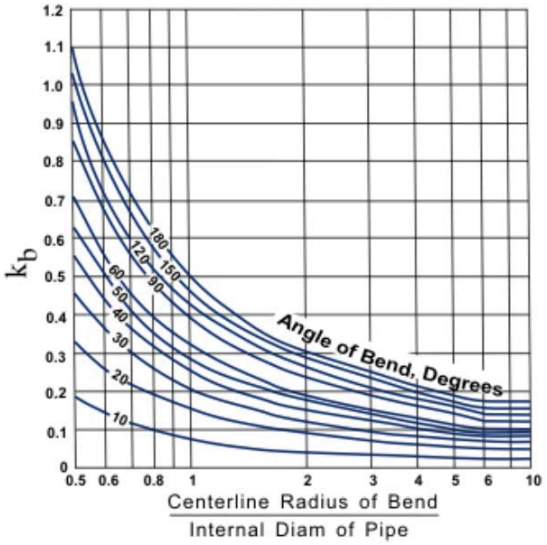

FIGURE 2.11. Bend loss coefficients for a pipe, see Kitto & Stultz (1978).

$$\frac{p_2}{p_1} = (\frac{\rho_2}{\rho_1})^{\gamma} = (\frac{T_2}{T_1})^{\gamma/(\gamma-1)} \tag{2.17}$$

where γ is the ratio of the heat capacity at constant pressure (C_P) to heat capacity at constant volume (C_V) and is considered to be 1.4 for dry air. This relation is valid for flows with small entropy variations (i.e. low viscosity and weak shocks). Under this assumption the total temperature, T_0, total pressure, p_0, and the total density, ρ_0, in a compressible flow are defined by the following relations:

$$\frac{T_0}{T} = 1 + \frac{\gamma - 1}{2} M^2; \tag{2.18}$$

$$\frac{p_0}{p} = (1 + \frac{\gamma - 1}{2} M^2)^{\gamma/(\gamma-1)}; \tag{2.19}$$

$$\frac{\rho_0}{\rho} = (1 + \frac{\gamma - 1}{2} M^2)^{1/(\gamma-1)}; \tag{2.20}$$

where T, p and ρ are the static values for temperature, pressure, and density, respectively at a point in the flow of a certain Mach number M. In an isentropic flow, the total temperature, pressure, and density, T_0, p_0, ρ_0 are constant throughout the flow domain. However, in an actual flow problem, like

the exhaust flow through the exhaust valve, there are flow losses due to the dissipative mechanisms of viscosity, thermal conduction, and diffusion.

Typically, engine engineers consider in one dimensional engine simulations the departures from the equivalent ideal flow by using the discharge coefficient C_D, see e.g. Fredrik *et al.* (2003) and Baratta *et al.* (2010).

2.2.7. *Discharge Coefficient of exhaust valves*

The discharge coefficient through an exhaust valve is defined as the ratio of actual mass flow rate, $\dot{m}_{real}$, and the ideal (theoretical) mass flow rate,$\dot{m}_{ideal}$, see equation 2.21:

$$C_D = \frac{\dot{m}_{real}}{\dot{m}_{ideal}} \tag{2.21}$$

where the actual mass flow rate can be measured by experiments. The ideal mass flow is calculated by

$$\dot{m}_{ideal} = \frac{A_R p_0}{\sqrt{RT_0}} (\frac{p_T}{p_0})^{\frac{1}{\gamma}} \{ \frac{2\gamma}{\gamma - 1} [1 - (\frac{p_T}{p_0})^{\frac{\gamma-1}{\gamma}}] \}^{\frac{1}{2}} \tag{2.22}$$

When the flow is choked, the equation 2.23 has to be used:

$$\dot{m}_{ideal} = \frac{A_R p_0}{\sqrt{RT_0}} \gamma^{\frac{1}{2}} (\frac{2}{\gamma + 1})^{\frac{\gamma+1}{2(\gamma-1)}} \tag{2.23}$$

where p_0 is upstream (cylinder) total pressure, T_0 is upstream (cylinder) total temperature, p_T is the static pressure at the flow restriction (gap between the valve and the seat), and a reference area A_R. The most convenient reference area, A_R, is the so called valve curtain area:

$$A_R = \pi D_v L_v \tag{2.24}$$

where D_v is the diameter of valve head and L_v is the valve lift, see Figure 2.2. In industry, the discharge coefficients of intake and exhaust valves are often measured on an airflow bench at low mass flows. There are some limitations in the process which are discussed in the following paragraph.

During airflow bench tests, the pressure difference between the in-cylinder and exhaust port is fixed at a given low value, typically between 10 to 28 inches of water (2.5 to 7 kPa). In reality, when the exhaust valves open, the pressure difference between the in-cylinder and the exhaust port region is over 500 kPa. Figure 2.12 shows the actual pressures in the cylinder and exhaust port of a whole Diesel engine cycle (data from 1D simulation by Aghaali & Angstrom (2013)). The pressure difference is about 580 kPa when the exhaust valves open. The temperature in an actual working engine is also much higher than the room temperature (used usually for the tests) and varies widely within the different components of the ICE. Obviously, the flow considered during

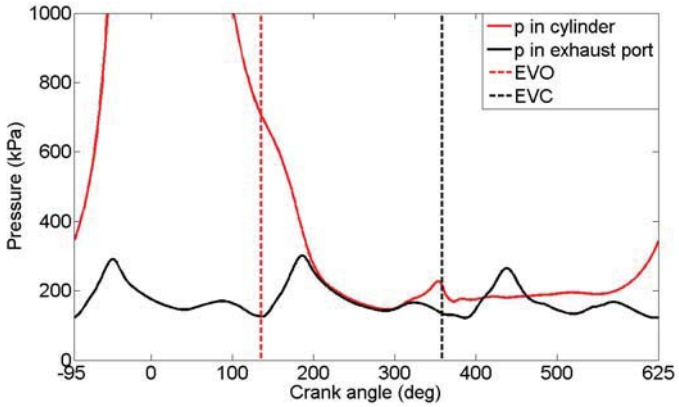

FIGURE 2.12. Actual pressures in the cylinder and exhaust port by one dimensional simulation. Red solid line, pressure in the cylinder. Black solid curve, pressure in the exhaust port. Red dash line, exhaust valve opening (EVO). Black dash line, exhaust valve closing. Data from Aghaali & Angstrom (2013).

the airflow bench does not have these characteristics, i.e. very high and wide range of pressures and temperatures. Due to high pressure difference, the flow through the exhaust port can easily be sonic with choked flow occurring. Moreover, the movements of piston and exhaust valves significantly have an effect on the flow conditions in an actual working engine which cannot be mimicked in airflow bench tests. The movement of piston could cause air to flow in strong pulses like conditions, as compared with the steady stream flow in an airflow bench situation.

Considering the strict definition of the discharge coefficient, equation 2.21 and equation 2.22, p_T is the static pressure at the flow restriction. However, it is difficult to measure this quantity at that particular location due to the complexity of the geometry. In some experiments, only a pressure drop between the in-cylinder pressure and the environmental pressure is measured (Decker (2013)). The pressure is recovered in the downstream of the exhaust port and an exhaust exit piece (like a diffuser).The measured pressure drop is the total pressure loss in the downstream. Due to the complex geometry of exhaust port, the downstream has a profound effect on the flow in the exhaust port.

2.3. Utilization of exhaust gas energy

The ability to utilize the energy in the exhaust gases may have a large impact on the total performance of the engine. Turbocharging is one way to utilize the otherwise wasted exhaust energy in the exhaust gases. It is one of the

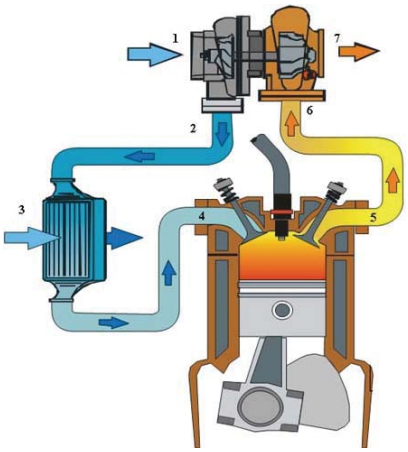

FIGURE 2.13. A schematic drawing of a turbocharging system (Electra (2010)): 1: Compressor Inlet, 2: Compressor Discharge, 3: Charge air cooler, 4: Intake Valve, 5: Exhaust Valve, 6: Turbine Inlet and 7: Turbine Discharge .

oldest waste heat recovery measures for ICEs (Watson & Janota (2005)). A turbocharger is a turbine-driven compressor, which forces air into the ICE to increase power output. Its main components are: a turbine, a compressor, shaft and bearing assemblies. Figure 2.13 shows the schematics of a turbocharging system (Electra (2010)). The exhaust gases ones passing through the high resistance exhaust port, they expand through the turbine to drive the compressor. The compressor compresses the incoming fresh air, increasing its pressure and density. However, the compression process produces heat and the temperature affects the density of the air. As the temperature rises, the oxygen content in a given space is reduced. A charge air cooler is commonly used to decrease the temperature of the compressed intake air and further increase the air density. With more air containing oxygen, more fuel can be combusted, which will increase the power output of the engine. On another hand, using turbochargers may allow to have a smaller engine with the same power output (engine downsizing).

The principle of utilization of exhaust gas energy can also be explained by the pressure-volume diagram in Figure 2.14. When the exhaust valves open at point 4, the gases in the cylinder have high pressure and temperature. Process 4-5-6 is the exhaust stroke. If the gases will be allowed to expand in the cylinder further down to point 9, the energy in the blow-down pulse (area 4-9-10) can be estimated. This is energy in the exhaust gases which could be theoretically recovered. A turbocharger system may be used with this purpose.

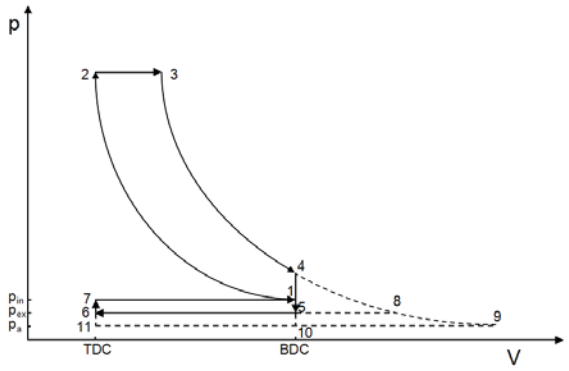

FIGURE 2.14. A p-V diagram of idealized turbocharged engine .

There are mainly two ways for a turbine system to operate with a constant pressure or pulse pressure system (Baines (2005)). If the manifold volume is large enough to damp out any pulsations from the exhaust valve event, then it is a constant pressure system. When the exhaust valve opens at point 4, the gas expands through the valve to point 5. The pressure in the turbine inlet keeps at a constant value. The advantage is that the turbine will work under steady state conditions for which it can be optimized and a higher efficiency during the whole exhaust stroke 4-5-6. Hence, a part of the exhaust energy (4-9-10) can not be utilized in turbine. Another way is to use a pulse pressure turbine system. The manifold volume is minimum and the pressure pulsations are not damped out. During the blow down phase (4-5), the turbine inlet pressure will fall from point 4 to 9 recovering the whole blow down energy theoretically. In process 5-6, the scavenging phase, the pressure in the cylinder keeps at p_{ex} . The ambient pressure p_a is lower than p_{ex}. The gas out of the cylinder expands in the turbine with a theoretically avail energy 5-10-11-6. The pulse pressure system is commonly used in four stroke engines.

For current automotive applications, there is room to improve the turbocharging system. As the ICE exhaust flow parameters change widely under a range of operating conditions, turbine working performances are impacted by the changes in the exhaust flow. Matching an ICE with a turbocharger system is a challenging task. Since the turbine is a rotational device, its optimal and highest efficiency operating condition is during steady state flow with a certain mass flow and pressure ratio. Therefore, the turbine operates with its highest efficiency only for a part of the whole duration of the engine cycle (Watson & Janota (2005)). One question which rises is concerning the valve opening/closing strategy used on the turbine performance. Another question

is related to the losses in the exhaust manifold and their effects on the turbine performance.

CHAPTER 3

Turbulence and Turbulence Modeling

The laws governing the fluid motion and the corresponding flow governing equations, equations 2.1 to 2.4, have been given in Section 2.2.2. Most flows encountered in everyday life experience are turbulent and turbulence is a topic of very high interest within fluid physics research. This chapter gives an overview on turbulence and turbulence modeling issues within the context of ICE related flows.

3.1. Turbulence

The flow in the exhaust port and manifold is essentially a (non-straight, variable cross-sectional) pipe flow. It is dominated by turbulence. Turbulence in pipe flows was experimentally observed for the first time by Osborne Reynolds (Reynolds (1883)). He carried out his famous experiments in 1883 highlighting the different flow regimes (i.e. laminar, transitional or turbulent) in a pipe flow. The water flow behavior in a glass tube was visualized by injecting dye into the water stream. At a very low velocity, the flow in the tube stayed laminar, i.e. streamlined, smooth and steady. The parallel streamlines were found to follow the axis of the tube. As the velocity was increased, small disturbances, individual eddies-like structures were observed. Increasing furthermore the velocity, these initial small disturbances started growing and regions with intense rotational structures were developed. This was the transitional regime from a laminar to a turbulent flow. Reynolds observed that the character of the flow was dependent on a certain dimensionless number, later named as the Reynolds number Re defined as:

$$Re = \frac{\rho U L}{\mu} \tag{3.1}$$

where ρ is the fluid density, μ is the dynamic viscosity of the fluid, U is a characteristic velocity scale, and L is a characteristic length scale (e.g. the diameter of the tube in Reynolds experiments). Reynolds number gives a measure of the ratio between the inertial forces to viscous forces. Under a certain critical Reynolds number the flow remains laminar (dominated by the viscous forces) and above this critical Reynolds number turbulence may occur.

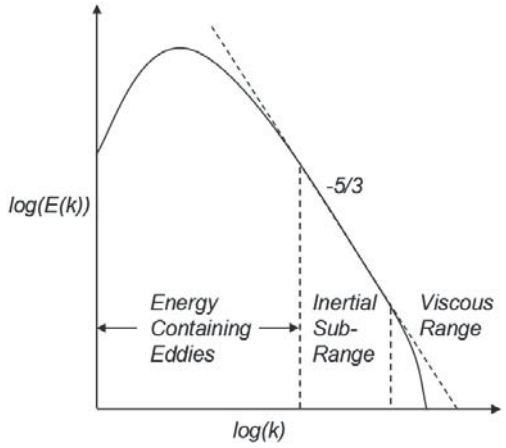

FIGURE 3.1. A typical energy spectrum of an ideal turbulent flow.

The transition from a laminar to a turbulent flow in a pipe occurs over a range of Reynolds numbers (2000 - 3000), e.g. (Johansson & Wallin (2012)). As the Reynolds number is increased and exceeds Re 4000, the flow in the tube becomes fully turbulent (Pope (2000)). A critical Reynolds number is only indicative in many cases since the presence of perturbation may trigger transition by different mechanisms and other Reynolds numbers then the commonly defined as the critical one.

3.1.1. *Properties of Turbulence*

Turbulence is a property of the flow and not a property of the fluid. There is no clear or complete definition on what turbulence is. However, scientists identified certain characteristics for turbulence which are used for identifying such flows.

A simple "definition" of turbulence is given by Kundu as a dissipative flow state characterized by nonlinear three-dimensional vorticity (Kundu *et al.* (2012)). Although the definition is not exclusive, it presents the generic characteristics of turbulence: fluctuations, nonlinearity, vorticity, dissipation and diffusivity.

In a turbulent flow, the developed turbulence structures are thought to be the characteristic scales of the flow motion. The large scales are determined and are limited by the geometry of the flow domain (e.g. one cannot have a larger vortical structure in the cross-section of a pipe than the pipe's diameter). Such structures have velocity and length scales of the same order as the mean flow. They interact most strongly with the mean flow extracting energy from the mean flow. The eddies interact with each other as long as their size is

comparable. Through this interaction energy is transferred from the mean flow to the small eddies where viscous dissipation is important and the kinetic energy of the eddies is converted to heat.

This process results in the so called turbulent energy cascade explaining how energy is transferred from the largest (integral scales) to the smallest structures (Kolmogorov micro-scales) of the flow. This can be illustrated in a schematic plot, see Figure 3.1. One should also note that this cascading process describe the average energy flow from large to small scales. Instantaneously, there is energy transfer from small to larger scales by merging of vortices. Such phenomena can be observed at all scales (e.g. merging of the initial axi-symmetric eddies in a turbulent jet flow close to the nozzle). Energy transfer from small to larger scales is called "back scatter" and is most often associated to small scale process that one would like to include in sub-grid-scale (SGS) models for LES.

Within the Kolmogorov theory, one may assume equilibrium between the production of turbulence kinetic energy and its dissipation. Thus, $\epsilon = -dk/dt$, where k is the turbulent kinetic energy per unit volume and epsilon is the dissipation rate of turbulent kinetic energy per unit volume (e.g. Pope (2000), Lee *et al.* (1997)). Using dimensional arguments one can estimate the length η_k, time τ_k, and velocity v_k for the Kolmogorov scales as follows:

$$\eta_k \equiv (\frac{\nu^3}{\epsilon})^{\frac{1}{4}}, \tau_k \equiv (\frac{\nu}{\epsilon})^{\frac{1}{2}}, v_k \equiv (\nu\epsilon)^{\frac{1}{4}} \tag{3.2}$$

where ν is the kinematic viscosity of the fluid.

An important feature of turbulent flows is their enhanced diffusivity and mixing as compared to corresponding laminar flows. The transfer of mass, momentum and energy are greatly enhanced by turbulent diffusion.

The chaotic character of turbulence makes it difficult to describe. Thus, the basic theory of turbulence is related to its statistical description. It is only in statistical terms that one can compare turbulent flows. Instantaneous data cannot be compared due to the chaotic character of the flow. Hence, the fluctuation that are not handled by the statistical methods being used has to be added, if one is interested of these by other means. In fact this is the situation both with experiments and modeling. In experiments the current measuring techniques the rate of gathering data (space- and time resolution) is limited to cases with relative large scales. In simulation the situation is similar: completely resolved simulation (so called Direct Numerical Simulations, DNS) is limited to flows with relatively large small scales, which is characterized by relatively low Reynolds numbers. For larger Reynolds numbers one has to use models to account for the unresolved components. Unfortunately, as already pointed out there are no experiments that can provide validating data

for corresponding Reynolds numbers due to the lack of appropriate measuring techniques and data transfer capacity.

3.2. Direct Numerical Simulations, DNS

For certain flow scenarios, the flow governing equations (equations 2.1 to 2.4) can be solved directly and three-dimensional, time-dependent numerical solutions can be computed, provided that all the scales of the flow are resolved. Since there are no models employed, the calculated solutions are numerically accurate values of the given flow problem. The required resolution implies also limitation on the largest possible Re for a given geometry and given computer. One may estimate the largest Re that can be resolved by estimating the computational work needed. If one assumes that the needed resolution in each direction is of the same order then the required number of computational cells is $O(Re^{3/4})$. Thus in 3D this would mean computational effort of $O(Re^{9/4})$. Since the time scale has to be such that a fluid particle moves less than one cell in a time step, this would imply that the number of time steps is $O(Re^{3/4})$, which altogether leads to an estimate of computational effort of the order of $O(Re^3)$. This strong dependence on Re makes DNS to be limited to low Reynolds number flows and simpler geometries.

Alternatives to the expensive DNS calculations are using the Reynolds Averaged Navier-Stokes (RANS) with the correspondent turbulence models or the more accurate Large Eddy Simulation (LES) approach. These are also the computational tools which have been used within present research study.

3.3. Turbulence modeling

3.3.1. *Reynolds Averaged Navier-Stokes*

Reynolds Averaged Navier-Stokes (RANS) is the most popular computational formulation used for handling turbulent flow characteristic to engineering problems. Within RANS framework the instantaneous flow variables (e.g. pressure, velocity) can be decomposed into a mean part and a fluctuating part:

$$p \equiv \bar{p} + p', u_i \equiv \bar{u_i} + u_i' \tag{3.3}$$

where an overbear denotes Reynolds average.

If this Reynolds decomposition is applied to the incompressible Navier-Stokes equations, the RANS equations of incompressible flows can be obtained. However, for a compressible flow the velocity components and the thermal variables (e.g. temperature and enthalpy) are mass (density weighted)-averaged by using Favre decomposition. The pressure and density are treated using the

Reynolds decomposition:

$$\left.\begin{aligned} p &= \bar{p} + p' \\ u_i &= \tilde{u}_i + u_i'' \\ \rho &= \bar{\rho} + \rho' \\ h &= \tilde{h} + h'' \\ e &= \tilde{e} + e'' \\ T &= \tilde{T} + T'' \\ q_j &= q_{L_j} + q_j' \end{aligned}\right\} \tag{3.4}$$

where an tilde denotes Favre (mass) average, $\bar{\rho}\tilde{u}_i = \overline{\rho u_i}$. Substituting Equations (3.4) into Equations (2.1) - (2.4), the Favre (mass) averaged mean conservation equations are derived:

$$\frac{\partial \bar{\rho}}{\partial t} + \frac{\partial(\bar{\rho}\tilde{u}_i)}{\partial x_i} = 0 \tag{3.5}$$

$$\frac{\partial(\bar{\rho}\tilde{u}_i)}{\partial t} + \frac{\partial(\bar{\rho}\tilde{u}_i\tilde{u}_j)}{\partial x_j} = -\frac{\partial \bar{p}}{\partial x_i} + \frac{\partial}{\partial x_j}(\bar{\sigma}_{ji} - \overline{\rho u_j'' u_i''}) \tag{3.6}$$

$$\begin{aligned} &\frac{\partial}{\partial t}(\bar{\rho}(\tilde{e} + \frac{1}{2}\tilde{u}_i\tilde{u}_i) + \frac{1}{2}\overline{\rho u_i'' u_i''}) + \frac{\partial}{\partial x_j}(\bar{\rho}\tilde{u}_j(\tilde{h} + \frac{1}{2}\tilde{u}_i\tilde{u}_i) + \tilde{u}_j\frac{1}{2}\overline{\rho u_i'' u_i''}) \\ &= \frac{\partial}{\partial x_j}(\tilde{u}_i(\tilde{\sigma}_{ji} - \overline{\rho u_i'' u_i''})) + \frac{\partial}{\partial x_j}(-q_{L_j} - \overline{\rho u_j'' h''} + \overline{\sigma_{ij} u_i''} - \overline{\rho u_j'' \frac{1}{2} u_i'' u_i''}) \end{aligned} \tag{3.7}$$

$$\bar{p} = \bar{\rho} R \tilde{T} \tag{3.8}$$

The last term in the mean momentum equation (3.6),$-\overline{\rho u_i'' u_j''}$, is the Favre-averaged Reynolds-stress tensor and can be rewritten as equation (3.9). The term, $\frac{1}{2}\overline{\rho u_i'' u_i''}$, in the mean energy momentum equation is the kinetic energy per unit volume of the turbulent fluctuations and can be rewritten as (3.10).

$$\bar{\rho}\tau_{ij} = -\overline{\rho u_i'' u_j''} \tag{3.9}$$

$$\bar{\rho}k = \frac{1}{2}\overline{\rho u_i'' u_i''} \tag{3.10}$$

The non-linearity of the equations results in new terms on the RHS of equations 3.5-3.8. These terms cannot be expressed directly in terms of the mean variables. Yet they have to be expressed somehow in terms of the mean variables (which are the knows if the RHS would be known). In the momentum equation the RHS consists of the divergence of the so called Reynolds stresses. Most effort has been put in modeling these terms. Yet the corresponding terms in the energy equation may be equally important.

TABLE 3.1. Coefficients used in RANS model

$C_{1\epsilon}$	$C_{2\epsilon}$	C_μ	σ_k	σ_ϵ	C_t
1.44	1.92	0.09	1.0	1.3	1

The RANS model used within this study is the two-equation standard $k-\epsilon$ turbulence model, in which the turbulent viscosity is evaluated as:

$$\mu_T = \bar{\rho} C_\mu \frac{k^2}{\epsilon} \tag{3.11}$$

where C_μ is a model constant, while k and ϵ are the turbulent kinetic energy and turbulent dissipation, respectively. Transport equations for k and ϵ can be solved for calculating the two variables:

$$\frac{\partial(\bar{\rho}k)}{\partial t} + \frac{\partial(\bar{\rho}k\tilde{u}_j)}{\partial x_j} = \frac{\partial}{\partial x_j}((\mu + \frac{\mu_T}{\sigma_k})\frac{\partial k}{\partial x_j}) + P_k - \bar{\rho}\epsilon - Y_M \tag{3.12}$$

$$\frac{\partial(\bar{\rho}\epsilon)}{\partial t} + \frac{\partial(\bar{\rho}\epsilon\tilde{u}_j)}{\partial x_j} = \frac{\partial}{\partial x_j}((\mu + \frac{\mu_T}{\sigma_\epsilon})\frac{\partial \epsilon}{\partial x_j}) + C_{1\epsilon}\frac{\epsilon}{k}P_k - C_{2\epsilon}\bar{\rho}\frac{\epsilon^2}{k} \tag{3.13}$$

where P_k is the production term of k as follows

$$P_k = \bar{\rho}\tau_{ij}\frac{\partial \tilde{u}_j}{\partial x_i} \tag{3.14}$$

and Y_M is the dilatation dissipation term due to the compressibility.

The Boussinesq hypothesis is used to model the Reynolds Stress tensor (3.15):

$$\bar{\rho}\tau_{ij} = -\overline{\rho u_i'' u_j''} = 2\mu_T(\tilde{S}_{ij} - \frac{1}{3}\frac{\partial \tilde{u}_k}{\partial x_k}) - \frac{2}{3}\bar{\rho}k\delta_{ij} \tag{3.15}$$

The turbulence heat flux vector is modeled as (3.16):

$$q_{T_j} = \overline{\rho u_j'' h''} = -\frac{\mu_T c_p}{Pr_T}\frac{\partial \tilde{T}}{\partial x_j} \tag{3.16}$$

The molecular diffusion and turbulent transport terms are modeled as (3.17):

$$\overline{t_{ji}u_i''} - \overline{\rho u_j''\frac{1}{2}u_i''u_i''} = (\mu + \frac{\mu_T}{\sigma_k})\frac{\partial k}{\partial x_j} \tag{3.17}$$

And the dilatation dissipation term Y_M is modeled according to Sarkar & Balakrishnan (1990) as:

$$Y_M = \frac{C_M k\epsilon}{c^2} \tag{3.18}$$

where $C_M = 2$, and c is the speed of sound. The model coefficients are given in Table 3.1, CD-Adapco (2011*a*).

In order to apply a two-equation turbulence model to a wall-bounded flow problem, the appropriate boundary conditions must be specified near by the solid boundary for the velocity and for the two turbulence variables. In terms of the velocity at the mesh point closest to the surface, the standard law of the wall can be regarded as:

$$u^+ = \begin{cases} y^+ & y^+ \leqslant y_m^+ \\ \frac{1}{\kappa} ln(Ey^+) & y^+ > y_m^+ \end{cases} \tag{3.19}$$

where the default values of the coefficient are κ =0.42, E= 9.0, y_m^+ is at the intersection of viscous and fully turbulent regions.. And the non-dimensional quantities are:

$$y^+ = \frac{yu^*}{\nu} \tag{3.20}$$

Thus, the mean velocity can be calculated by:

$$\tilde{u} = u^+ u^* \tag{3.21}$$

The reference is often related to the wall shear stress.

$$u^* = \sqrt{\tau_w/\rho} \tag{3.22}$$

The wall shear stress is given by:

$$\tau_w = \mu(\frac{\partial u}{\partial y})_{y=0} \tag{3.23}$$

where μ is the dynamic viscosity, u is the flow velocity parallel to the wall and y is the distance to the wall.

3.3.2. *Large Eddy Simulation*

Large Eddy Simulation (LES) is an approach which resolves the large (energy containing) scales and models only the smallest, so called subgrid-scale (SGS) eddies. While RANS models the full range of turbulent scales, LES models only the part of the scales which cannot be solved by the computational grid. This is a step towards DNS where all the scales are resolved. Therefore, more flow structures can be accurately represented in the flow field by LES as compared with RANS. Moreover, the dynamics and the fluctuations in the turbulent flow are better captured.

However, in the same time, as compared with DNS, LES requires much less computational cost because the filter width used (grid size) can be much larger than the Kolmogorov length scale. A comparison between DNS (Lee *et al.* (1997)) and LES (Akselvoll & Moin (1993)) calculations has been done of a backward facing step flow at low Reynolds number of 5000. The results show that LES required 3% of the number of grid points necessary for the DNS and

that the LES computer time was 2% of that for the DNS with good agreement with the experiment.

For compressible flow, the instantaneous velocity can be separated by Favre filtering method into two parts:

$$u_i = \tilde{u}_i + u_i'' \tag{3.24}$$

Here, the averages represent the spatial filtering in LES and not the ensemble averaging used for the RANS formulation. Thus, $\tilde{u}_i$ is the filtered velocity in LES and u_i'' is the subgrid velocity. Both $\tilde{u}_i$ and u_i'' are dependent on the filter size and the impact of modeling in LES should decrease as the filter size decreases. If the filter size decreases to the Kolmogorov length, LES will turn to DNS. By applying the Favre filter to the momentum equation (2.2), one can get the filtered LES equations (3.26), see e.g. Wilcox (2006):

$$\frac{\partial(\bar{\rho}\tilde{u}_i)}{\partial t} + \frac{\partial(\bar{\rho}\tilde{u}_i\tilde{u}_j)}{\partial x_j} = -\frac{\partial \bar{p}}{\partial x_i} + \frac{\partial}{\partial x_j}(\bar{\sigma}_{ji} + \bar{\rho}\tau_{ij}) \tag{3.25}$$

where

$$\tau_{ij} = -(\widetilde{u_i u_j} - \tilde{u}_i\tilde{u}_j) \tag{3.26}$$

Comparing the sub-grid stresses to the Reynolds stress, it is clearly a different physical meaning. However, both the Sub-Grid Stresses (SGS) and Reynolds stresses cannot be expressed in terms of averaged variables and has to be modeled. Yet, there is a major difference between the Reynolds stresses and the SGS terms. The former models *all* the turbulent scales and hence is independent of the spatial resolution that one uses. On the other hand the SGS terms are getting smaller as the filter size (Δ) is reduced. In fact the approximation error of the SGS (i.e. the size of the SGS) is proportional to Δ^2. Thus, LES is in fact an approximation in a mathematical sense whereas the Reynolds stress requires modeling independently to the numerical resolution. Different SGS models have been proposed within LES framework. For example, within the Smagorinsky model (Smagorinsky (1963)) the SGS are modeled by a Boussinesq assumption as follows:

$$\tau_{ij}^r = -2\nu_T \bar{S}_{ij} \tag{3.27}$$

where τ_{ij}^r is the anisotropic portion of τ_{ij}, see e.g. Pope (2000). The turbulent eddy viscosity ν_T is modeled like:

$$\nu_T = l_S^2(2\bar{S}_{ij}\bar{S}_{ij})^{1/2} \tag{3.28}$$

where l_S is the Smagorinsky length scale, $l_S = C_S\triangle$, $\triangle$ is the mesh length scale and $(2\bar{S}_{ij}\bar{S}_{ij})^{1/2}$ is the characteristic the characteristic filtered rate-of-strain. C_S represents the Smagorinsky constant. Generally, the Smagorinsky model is considered to be too dissipative in particular for low Reynolds number flows, see e.g.Pope (2000).

As comparing to RANS, more flow structures are represented within a LES flow field. This is due to the way in which the non-linear terms, i.e. $\frac{\partial(\bar{\rho}\tilde{u}_i\tilde{u}_j)}{\partial x_j}$, in the momentum equation (3.26) are treated within LES framework. The non-linear terms must be allowed to function sufficiently to let the flow structures increase. There are two methods to achieve this function: less dissipative turbulence models or a denser grid (Rutland (2011)).

If a grid is fine enough (i.e. resolving a portion of the inertial subrange whereby the dissipative part of the spectrum is disconnected from the equilibrium subrange), the inherent numerical dissipation can be used to account for the dissipative effect at the level of the smallest scales. It has been used by many researchers for a number of years and in many applications, e.g. for example Garmann *et al.* (2013), Margolin *et al.* (2006). This LES is commonly called Implicit LES. Consider the simplified transport equation:

$$\frac{\partial u}{\partial t} + \frac{\partial F(u,x)}{\partial x} = 0 \tag{3.29}$$

The filtering operation introduces the sub-grid scale term, called SGS below, to the equation which now is for the filtered variable $\tilde{u}$.

$$\frac{\partial \tilde{u}}{\partial t} + \overline{\frac{\partial F(u,x)}{\partial x}} = \overline{\frac{\partial F(u,x)}{\partial x}} - \frac{\partial F(u,x)}{\partial x} = SGS \tag{3.30}$$

When the equation (3.31) is discretized, another rest term is introduced which contain the truncation errors, T, associated with the particular scheme used.

$$\frac{\partial \tilde{u}}{\partial t} + \overline{\frac{\partial F(u,x)}{\partial x}} = SGS + T \tag{3.31}$$

Normally, the SGS term must, in order for the LES to produce reasonable results, account for the behavior of the fluid scales that it filters away. One motivation for implicit LES is that this dissipative nature is something which these scales share with stable numerical schemes. And, since the effect of the SGS and T terms are additive, their total effect may be accounted by the numerical scheme, T. Of course, this approach makes the dissipation completely dependent on the grid and the numerical scheme. Yet, if there is a resolved equilibrium subrange the effect of the error due to excessive dissipation, is not propagating to the larger resolved scales, as it should be for large eddy simulation.. The benefits are simplicity and low computational costs since no SGS model is used. In addition, one can argue that there is no unwanted dissipation present.

CHAPTER 4

Numerical Methods for Exhaust Flow Modeling

The flow governing equations form a system of non-linear partial differential equations (PDE). These equations may be solved analytically only under severe simplifying assumptions, otherwise no general analytical solutions can be found. Numerical techniques are commonly used to solve approximately the set of PDEs. The basic approach is to discretize the dependent variables in space and time and then express the dependent variables in terms of multi-dimensional local polynomials or global functions (such as Fourier modes). The former approach results, when applied to the spatial variations of the dependent variables in finite difference, finite element and finite volume approximations. The latter approach results yields the spectral method that has been popular for DNS of channel and other flows in periodic geometries.

In the present work, all the simulations are performed by using finite volume based commercial flow solvers provided by CD-adapco Co. (i.e. STAR-CCM+ 7.06 and STAR-CD 4.16 by CD-Adapco (2011*a*)). Most of the work was carried out using the STAR-CCM+ solver. However, for simulating the complex movement mechanism of the piston and the valves, the STAR-CD solver was employed.

The finite volume method involves several steps. It is formulated to allow unstructured meshes and is suitable for handling complex geometries as the exhaust port is. These steps are:

1, The solution domain is sub-divided into a finite number of control volumes;

2, The dependent variables are approximated on each element (so called control volume) by a local polynomial. The governing equations ban be integrated over each finite control volume. The integration leave the coefficients of the polynomials as unknowns. The temporal discretization can be done in a similar manner.

3, The set of PDEs becomes a set of non-linear algebraic equations;

4, Due to its non-linearity the system of the algebraic equations is solved using iterative methods.

The first step is completed by making a mesh for the computational domain. In step 2, the governing equations (2.1- 2.3) are integrated over each control volume in the computational mesh as follows:

$$\frac{\partial}{\partial t}\int_V W dV + \oint [F - G] dA = \int_V H dV \tag{4.1}$$

where,

$$W = \begin{Bmatrix} \rho \\ \rho u_1 \\ \rho u_2 \\ \rho u_3 \\ \rho(e + \frac{1}{2}u_i^2) \end{Bmatrix} \tag{4.2}$$

and F and G are the convective and diffusive parts of the fluxes,

$$F = \begin{Bmatrix} \rho u_i \\ \rho u_1 u_i + p\delta_{1i} \\ \rho u_2 u_i + p\delta_{2i} \\ \rho u_3 u_i + p\delta_{3i} \\ \rho u_i(h + \frac{1}{2}u_i^2) \end{Bmatrix} \tag{4.3}$$

$$G = \begin{Bmatrix} 0 \\ t_{i1} \\ t_{i2} \\ t_{i3} \\ u_j t_{ij} - q_i \end{Bmatrix} \tag{4.4}$$

and H contains source terms (e.g. body forces). The integrated equations on a control volume (cell 0), become:

$$\frac{\partial}{\partial t}(WV)_0 + \Sigma_f [(F - G)A]_f = (HV)_0 \tag{4.5}$$

where V is the cell volume and A is its surface, the subscripts 0, and f denote the value of the variable at some point within the volume and surface, respectively.

By their physical meaning, these terms are the transient term, the convective term, the diffusive term, and the source term. The approximations to the integrals require the values of variables at locations other than the computational nodes, i.e. in the center of the control volume.

4.1. Temporal discretization

The time-dependent term is only included in the transient (unsteady) calculations. A generic expression for the time evolution of a variable ϕ is given by

$$\frac{\partial \phi}{\partial t} = F(\phi) \tag{4.6}$$

where the function F incorporates any spatial discretization. In this thesis, all the simulations employ the second order implicit temporal scheme. It discretizes the transient term using the solution at the current time level, $n+1$, as well as those from the previous two time steps, n and $n-1$:

$$\frac{3\phi^{n+1} - 4\phi^{n} + \phi^{n-1}}{2\Delta t} = F(\phi^{n+1}) \tag{4.7}$$

This is referred to as an implicit integration since ϕ^{n+1} in a given cell is related to ϕ^{n+1} in the neighboring cells through $F(\phi^{n+1})$. The implicit equation can be solved iteratively at each time level before moving to the next time step. The advantage of the fully implicit scheme is that it is unconditionally stable with respect to time step size.

4.2. Spatial discretization

A second order accurate central difference discretization scheme was selected for the spatial discretization of convective term, diffusive term and source term. The central differencing scheme calculates the face value for a variable (ϕ_f) as follows:

$$\phi_{f,CD} = \frac{1}{2}(\phi_0 + \phi_1) + \frac{1}{2}(\nabla\phi_0 \cdot \vec{r}_0 + \nabla\phi_1 \cdot \vec{r}_1) \tag{4.8}$$

where the indices 0 and 1 refer to the cells. Cell 0 and cell 1 share face f. $\nabla\phi_0$ and $\nabla\phi_1$ are the reconstructed gradients at cell 0 and 1, respectively. $\vec{r}_0$ and $\vec{r}_1$ are vectors directed from the cell centroid toward the face centroid.

However, the central differencing schemes may produce non-physical oscillations. Therefore, in all the transient simulations performed, the Bounded Central-Differencing scheme (Leonard (1991),Darwish & Moukalled (1994)) available STAR-CCM+ has been used , while the Monotone Advection and Reconstruction Scheme (MARS) (Leer (1977),Zalesak (1979),Shyy (1994)) has been used with STAR-CD solver.

The Bounded Central-Differencing scheme is essentially based on the normalized variable diagram (NVD) approach (Leonard (1991)), together with the convection boundedness criterion (CBC). Thus, it is a composite NVD scheme that consists of a pure central differencing, a blended central differencing and a second-order upwind scheme, or a first order upwind scheme (only when the CBC is violated).

MARS is a multi-dimensional second-order accurate differencing scheme that operates in two separate steps, i.e. reconstruction and advection CD-Adapco (2011*b*). The reconstruction consists in computing a set of monotone gradients using a multi-dimensional Total Variation Diminishing (TVD) scheme. A second order accurate spatial discretization has been used during the computing process. The advection step consists in computing the fluxes with a monotone and bounded advection scheme. The advantage with MARS scheme is that as compared with other schemes available within the solver, the solutions accuracy is less sensitive to the structure of the mesh or to the skewness of the computational cells.

4.3. Boundary conditions

For solving the flow field, initial and boundary conditions for the flow variables are required. These should be specified in such a way that they represent the flow case under consideration. In this section the inlet, outlet, and wall boundary conditions used with the present calculations are outlined.

The flow at the inlet boundary is subsonic in all simulations. Four conditions are needed. With the present calculations two types of inlet boundary conditions were used, i.e. mass flow inlet and stagnation inlet.

Mass flow inlet boundary condition uses a specified mass flow together with a specified total temperature. The flow direction is assumed perpendicular to the boundary surface, which means the other two (in-plane) velocity components are zero. The axial velocity (normal to the boundary) is calculated by:

$$u_n = \frac{\dot{m}}{\rho A} \tag{4.9}$$

where ρ is the density and A is the boundary surface area and $\dot{m}$ is specified mass flow rate on the inlet surface. The static temperature, T, is calculated by the specified total temperature, T_{tot}, with the isentropic definition of total enthalpy. The Mach number can be calculated by

$$M = \frac{u_n}{c} \tag{4.10}$$

where c is the speed of sound, and with the isentropic relation, the total pressure can be calculated by

$$p_{tot} = p(1 + \frac{\gamma - 1}{2} M^2)^{\frac{\gamma}{\gamma - 1}} \tag{4.11}$$

Stagnation inlet boundary condition specifies the total temperature,T_{tot} and the boundary face total pressure,p_{tot}. Since the total pressure,p_{tot}, is given, the pressure can be extrapolated from the adjacent cell using reconstruction

gradients for subsonic flow. The static pressure,T, is obtained by:

$$T = \frac{T_{tot}}{(p_{tot}/p)^{R/C_p}} \tag{4.12}$$

With the assumption that the flow direction is normal to boundary surface, the axial velocity is obtained by:

$$u_n = \sqrt{2C_p(T_{tot} - T)} \tag{4.13}$$

Pressure outlet is the only boundary condition type used in all the simulations. It consists in applying a static pressure in the outlet surface.

If back-flow occurs, the pressure p at the boundary is given by:

$$p = p_{specified} - \frac{1}{2}\rho u_n^2 \tag{4.14}$$

where u_n is the normal component of the velocity at the boundary, which is extrapolated from the adjacent cells. This operation will prevent back-flow to occur.

The mesh is stretched in the direction normal to the outlet boundary in order to dissipate eventual back pressure pulses reflected from the outlet.

For the wall boundary conditions, no-slip velocity is specified in the computation domain. Another parameter is the temperature specification. There are mainly two ways: either by specifying the wall as an adiabatic wall or fixed at different temperatures.

4.4. Solution procedures

Two different solving algorithms are available within the STARCCM+, i.e. the semi-incompressible segregated solver and the fully compressible, coupled solver. In all the simulations involving STARCCM+, the fully compressible coupled solver is used. The coupled solver, or so-called density based solver, solves the governing equations of continuity, momentum, and energy and species transport simultaneously. Since the governing equations are non-linear, several iterations of the solution loop will be performed to get a converged solution.

There is no coupled solver within STAR-CD, only the segregated solver or so-called pressure based solver. This type of solver, can also provide adequate solutions for compressible flow situations. It solves the continuity and the momentum equations for a compressible flow in a separated manner. The pressure-velocity coupling is realized via a pressure based equation Barton (1998). In this research, the Pressure Implicit with Splitting of Operators (PISO) is used for unsteady moving mesh problems Versteeg & W.Malalasekera (1995).

CHAPTER 5

Solver Verification and Computational Cases

In the following sections, the different computational cases emphasizing the initial and the boundary conditions (BC) used and the reasons using these particular BC. The investigated situations can be separated into two categories of cases: i.e. "Laboratory-like condition" and "Engine-like condition".

Within "Laboratory-like condition" flow calculations, fixed valves and fixed inlet mass flow rate are considered. Moreover, the "Laboratory-like condition" calculations are not considering the temperature effects (i.e. "cold" flow calculations are performed). The boundary conditions are chosen to match the experiments carried out at SCANIA on the air flow bench using the same geometry. The experimental data obtained by SCANIA in terms of total pressure losses for different (fixed) valve lifts are used for comparison purposes. A grid sensitivity study has also been carried out so as to show grid convergence and for solver verification purposes.

All the "Engine-like condition" simulations takes into account elevated temperature but not the combustion process itself. However, the heat transfer to the walls is neglected. The "Engine-like condition" calculations are divided into three sub-groups. This is done for quantifying the effects that the different assumptions and simplifications may have on the exhaust "hot" flow and the associated losses. Note that problem simplifications are commonly associated with air flow bench experiments (e.g. "cold" flow assumption, fixed geometry and low pressure drop) and with simple simulation tools often used for assessing the exhaust flow.

5.1. Geometry

The geometry used in all the simulations presented in this thesis comes from the SCANIA heavy-duty Diesel engine, the D12. The geometry has been shown in Figure 2.3. There are two simplifications in this geometry. The first one is that the piston is considered to be flat (piston bowl effect not simulated) and it is simulated (in some cases) by imposing a constant mass flow inlet or stagnation pressure inlet. The second simplification is that the intake valves and ports are removed and are considered as closed part of the roof of the engine.

TABLE 5.1. Specifications of the internal combustion engine

Engine Label	Scania D12
Displacement (dm^3)	11.7
Bore (mm)	127
Stroke (mm)	154
Conn. Rod length (mm)	255
Compression ratio (mm)	18
EVO (CAD)	136
EVC (CAD)	359
Engine speed (rpm)	1200

In the cases in which the motions of the valves and the piston are considered (as part of "Engine-like condition" simulations), the piston or the valves will move based on pre-defined motion curves according to SCANIA. The details will be given within the next few sections. The general characteristics of the ICE in cause are specified in Table 5.1.

5.2. Simulated configurations

In this section, all the simulated cases will be described together with their initial, boundary conditions, and computational grids employed.

5.2.1. *Cases under "Laboratory-like condition"*

In "Laboratory-like condition" cases (see Table 5.2), the compressible "cold" flow calculations are performed to support the experiments carried out at SCANIA. Thus, the imposed boundary conditions are chosen to match those used during the experimental investigation. At the piston position (inlet plane in the computational domain), see Figure 2.3, the mass flow rate is imposed (constant or pulsatile). The combustion effect on temperature of the flow is not considered, the flow being cold with the air considered initially at standard room temperature (293 K). The outlet of the computational domain is kept at room, ambient temperature and constant atmospheric pressure conditions in accordance to the experiments. The walls are modeled as no-slip, adiabatic walls. The valve lifts are fixed at certain distances of respectively 3mm (L4 case), 4mm (L1-L3, L5), and 5mm (L6, L7), depending on the case.

For the cases L1 to L3 (the exhaust valves fixed at 4mm) the same mass flow at the inlet is considered (0.09 kg/s). However, these cases differ since different computational grid resolutions are employed (L1 - coarsest, L3 - the finest). Large Eddy Simulation (LES) calculations are performed on all three different grid resolutions for assessing the sensitivity of the flow solution to

TABLE 5.2. Overview of the Laboratory-like cases. Grid 1, 2, and 3 with an isotropic hexahedral core cell size of 1, 0.8, and 0.6 mm, respectively.

Case	Valve lift (mm)	Inlet mass flow (kg/s)	Grid
L1	4	constant 0.09	1
L2	4	constant 0.09	2
L3	4	constant 0.09	3
L4	3	constant 0.0664	3
L5	4	constant 0.0873	3
L6	5	constant 0.1	3
L7	5	pulse with mean value 0.1	3

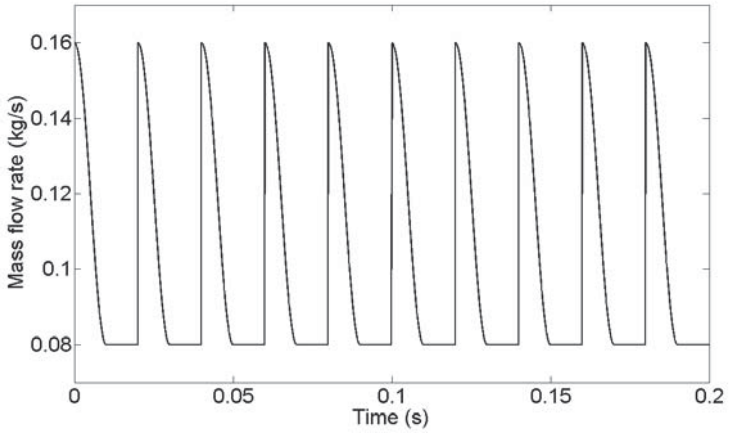

FIGURE 5.1. The pulse mass flow rate (10 cycles) in case L7. The mean value in each cycle equals 0.1 kg/s in case L6.

the chosen grid. The valve lift effect is considered running the cases L4 to L6. Three different mass flow rates (constant and not time-dependent) are imposed according to the values obtained from the experiments performed at the correspondent different valve lifts of 3, 4, and 5mm, respectively. Both LES and URANS calculations are carried out for L4, L5, and L6 cases for comparison purposes. The available experimental data (air flow bench data from SCANIA) are used for validation purposes (in terms of total pressure losses). The obtained LES results for these L4 to L6 cases, which will be detailed within the next chapter, will be used for presenting the overall exhaust flow field characteristics and associated structures. Case L7 differentiate itself

from the L6 case by considering at the inlet (piston) plane a time-dependent, pulsed mass flow condition instead of a constant one. The mass flow rate as a function of time is shown in Figure 5.1 for the first 10 cycles. In each cycle, the mass flow rate equals 0.1 kg/s, i.e. the same mass flow rate used with L6 case under a constant mass flow rate condition. For the L6 and L7 cases (with 5mm valve lift), the dominant flow structures are quantified using mode decomposition techniques. The purpose is to assess the effect of pulses on the flow structures and losses.

5.2.2. *Details of the computational grids*

Originally, a fully hexahedral computational mesh was supplied by SCANIA. The finest grid region within the whole computational domain was in region of the exhaust port, with the smallest computational cells located at the valve's gap (cell size of about 0.07 mm). The total number of mesh volumes was over three million with the SCANIA grid. This computational grid was used for the first URANS and LES simulations performed by the author, results presented in the first paper attached to this thesis (see attached paper). However, it turned out that it was difficult to refine and manipulate the grid when the motion of valves and piston was to be considered.

Thus, other three computational grids (Grid 1, 2, and 3 in Table 5.2) were generated using the same grid structure, with the coarsest one (Grid 1) having about 3 million mesh volumes and with the finest one (Grid 3) of about 10 million computational cells. They have an isotropic hexahedral core mesh in the exhaust port and two layers of prism cells at the walls. The corresponded computational sizes for the hexahedral core cells for each of the grids are 1 mm (Grid 1), 0.8 mm (Grid 2), and 0.6 mm (Grid 3). In the outlet region, cells are stretched in the direction normal to the outlet with an increasing ratio of 1.2 in order to damp the eventual pressure wave reflections from the outlet. For the prism layers, the total thickness equals half of the hexahedral core cell size and the growth ratio considered was 1.2.

A grid sensitivity study using these three different grids was carried out. The time-averaged axial velocity and its fluctuating component (RMS) were extracted for each of the mesh resolutions used along two orthogonal probe-lines located in a cross-section at y=5d, as shown in Figure 2.3.

Figure 5.2 shows the mean axial velocity profiles as calculated for Grids 1 to 3 along the orthogonal probe lines (along x and along z direction, respectively). As the mesh is refined the differences between the obtained solutions are getting smaller (within 5%). The same conclusion can result from analyzing the data obtained in terms of the axial velocity fluctuation (RMS), see Figure 5.3.

Power spectral density (PSD) plots based on time history data of axial velocity component calculated on the finest grid (Grid 3, L3) are shown in

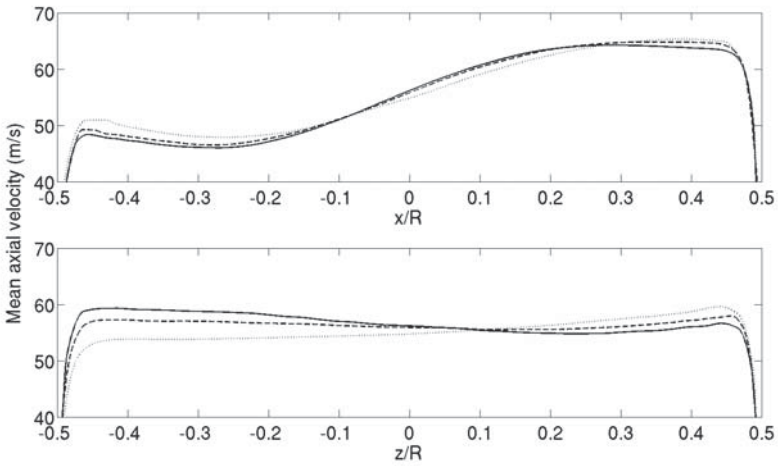

FIGURE 5.2. Grid sensitivity study: time-averaged axial velocity profiles over x (top row) and z (bottom row) at the cross section of y=5d (Figure 2.3). Grid 1, '$\cdots$' (Case C1 coarsest); Grid 2, '- -' (Case C2); Grid 3,'–'(Case C3, finest).

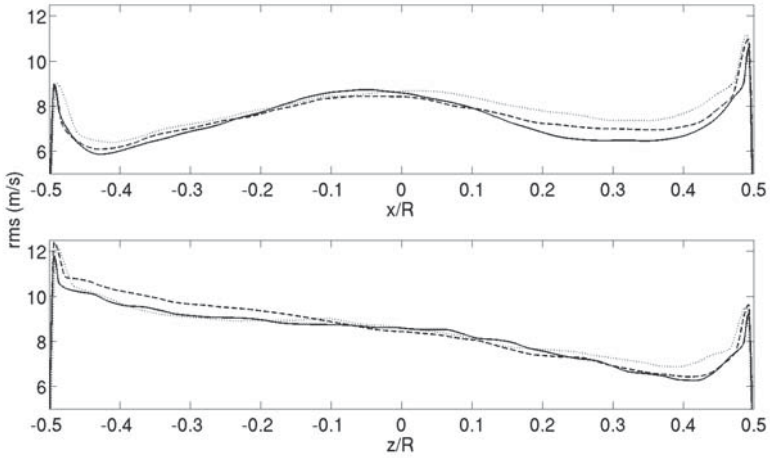

FIGURE 5.3. Grid sensitivity study: RMS of axial velocity profiles over x (top row) and z (bottom row) at the cross section of y=5d (Figure 2.3). Grid 1, '$\cdots$' (Case C1 coarsest); Grid 2, '- -' (Case C2); Grid 3,'–'(Case C3, finest).

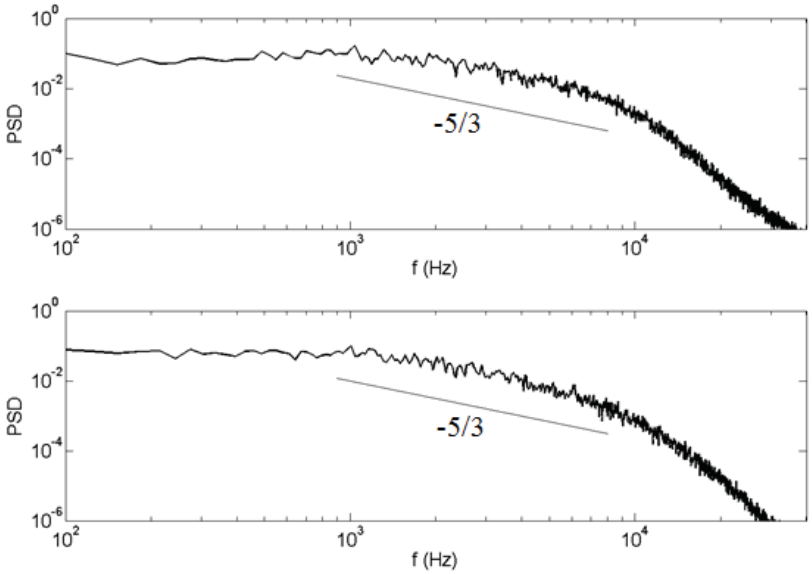

FIGURE 5.4. Power spectral density plots of the axial velocity component. PSD in point P1 (top) and PSD obtained in point P2 (bottom). Note the P1 and P2 locations in Figure 2.3 .

Figure 5.4. The spectra were calculated in two monitoring points, P1 and P2 specified at the locations as depicted in Figure 2.3. It can be seen that the grid resolution used is sufficient to solve a large part of the inertial sub-range, the spectra following for one order of magnitude the $-5/3$ slope associated with the turbulent energy cascade.

For all the "Engine-like condition" configurations the finest mesh (Grid 3 in Table 5.2), has been used. Additionally, an Arbitrary Lagrangian-Eulerian (ALE) mesh motion technique has been used in the cases involving valves or piston motion (Donea *et al.* (2004), Armero & Love (2003)).

5.2.3. *Cases under "Engine like condition"*

All the "Engine-like condition" cases considered the airflow as being "hot" as a result of the combustion process. However, all the solid surfaces are treated as isothermal walls at different temperatures (from gathered data). The "Engine-like condition" cases are divided into three sub-groups, representing different levels of simplification.

The first sub-group(see Sub-section 5.2.3a) considers the pressure at the outlet plane of the computational domain as constant static pressure. The two other sub-groups (presented in Sub-section 5.2.3b and Sub-section 5.2.3c) are

TABLE 5.3. Simulation cases in the test group.

Case	Piston or inlet	Valve	Pressure outlet
T1	Moving	moving	constant 200 kPa
T2	Moving	Fixed at 5mm	constant 200 kPa
T3	Stagnation pressure 340 kPa	Fixed at 5mm	constant 200 kPa
T4	Stagnation pressure 220 kPa	Fixed at 5mm	constant 200 kPa

considering pressure pulses at the outlet boundary associated with the exhaust flow. Thus, time-dependent pressure data provided by GT-Power simulations (Aghaali & Angstrom (2013)) are imposed for these two other sub-groups at the outlet plane.

In each of the three sub-groups, some of the cases include valves or piston motion. In the first two sub-groups (see Sub-section 5.2.3a and Sub-section 5.2.3b), the valves are not closed completely during their motion and only a part of the exhaust process in the internal combustion engine is considered, from 171 CAD to 324 CAD. The minimum valve lift considered is of 3.5 mm, while the maximum valve lift is of 14 mm.

The third sub-group (set-up detailed in the Sub-section 5.2.3c) consists in the most complex situation simulated here using the LES approach. It distinguishes from the other simulations (part of the first and the second sub-groups) by the fact that the exhaust valves are fully closing at the beginning and at the end of their motion. Thus, the whole exhaust process from 136 CAD to 359 CAD is simulated, allowing the exhaust valves to sit on their seats. Pulsed pressure boundary conditions are considered at the outlet plane of the computational domain.

5.2.3a. *Sub-group 1: Test group with "Engine like condition".* An overview of the simulated cases considered in the first sub-group is given in Table 5.3. All the simulations regarding the first sub-group (called a test sub-group) have been performed with assumed constant outlet pressure boundary condition, not including as outlet boundary condition the typical pressure pulses associated with the exhaust flow upstream of the turbo. However, when simulating the moving piston moving valves cases, the results showed that back-flow may occur at the outlet for certain CAD range (of about 25 CAD).

In these cases, the walls (including the valves) are assumed ideally smooth. No-slip condition for velocity is applied at the walls. Different wall temperature conditions are fixed for the different components: the piston at 600 K, the cylinder wall at 400 K, and the port wall at 500 K. The valves are assumed to behave adiabatic. At the outlet, a constant static pressure outlet boundary condition of 200 kPa is considered, resembling the back pressure due to the

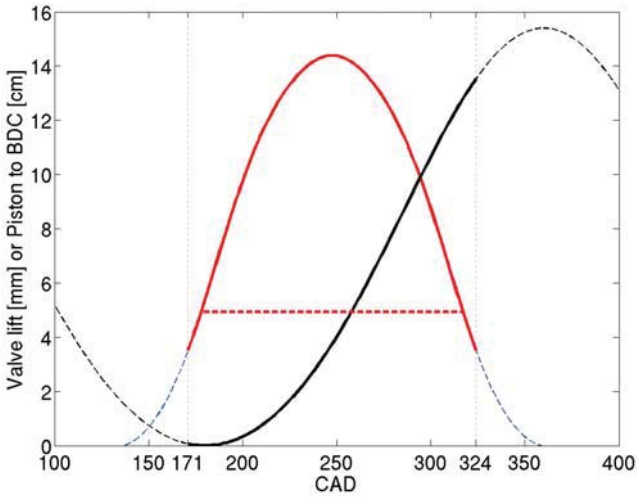

FIGURE 5.5. Piston and valve lifts are shown as a function of crank angle: illustrated in black the piston motion (cm); red displayed the valve lift (mm) for moving valve and moving piston cases; red dash line corresponds to the fixed valve lift at 5mm moving piston cases.

presence of the turbocharger. A static temperature 600 K is imposed (active only used if back-flow occurs).

The most complex approach is used for case T1, which includes the valve and piston motion. The valve and piston motion is handled as visualized in Figure 5.5. The piston follows the black solid curve from 171 CAD to 324 CAD. For the same CAD range, the exhaust valves move with the red solid curve. As can be seen in the Figure 5.5, the exhaust valves are not closed completely. The minimum valve lift considered is of 3.5 mm and only the part of the cycle from 171 CAD to 324 CAD is simulated. Thus, within the engine's cylinder, there will be always a jump in the piston motion during the LES calculations.

In order to calculate several cycles, the solution method employed was to keep the flow field from the previously computed cycle (data at 324 CAD) within the exhaust port and exhaust manifold as initial condition for the next, following cycle. This is illustrated in Figure 5.6. Only the in-cylinder data are forced at the beginning of each simulated cycle (i.e. a static pressure 390 kPa and a temperature of 820 K). All the flow data in the exhaust port and manifold are kept as calculated from the previous cycle.

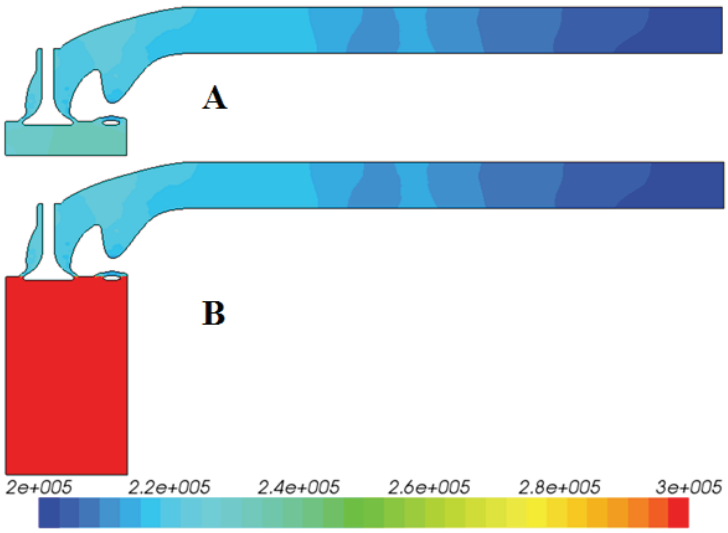

FIGURE 5.6. Illustration of the Initial conditions for each simulation cycle. A: Static pressure (Pa) distribution at 324 CAD the end of the last simulation. B: Static pressure (Pa) distribution at 171 CAD for the following simulation cycle.

A simplified approach is used with case T2, where the maximum valve lift is fixed at 5mm. The piston motion is modeled in the same fashion as for case T1. The motions of the exhaust valves begin at 171 CAD for a 3.5 mm valve lift (similar as for case T1). However, when they reach the 5 mm valve lift, the exhaust valves will be fixed for this value as shown by the the red dashed line in Figure 5.5. This case give a comparison with the moving valve and moving piston case.

The third modeling approach (and most simplified) is represented by the cases ignoring the motion of the valve and the piston, see case T3 and case T4 in Table 5.3. For these two, the valves are fixed at a certain valve-lift position of 5 mm and the piston is resembled by a total pressure source acting in the cylinder. By comparison, in the case T1, the valves can reach two times within a simulated cycle the valve lift of 5 mm, i.e. 178 CAD and 317 CAD. Therefore, for comparison purposes, the stagnation pressure in the case T3 imposed as boundary condition (340 kPa) equals the averaged stagnation pressure in the cylinder at 178 CAD as calculated in T1, which is 340 kPa. The considered temperature for the same reasons is 786 K. Similarly, the stagnation pressure in the case T4 imposed as inlet boundary condition (220 kPa) equals the averaged stagnation pressure in the cylinder at 317 CAD as calculated in T1, which is

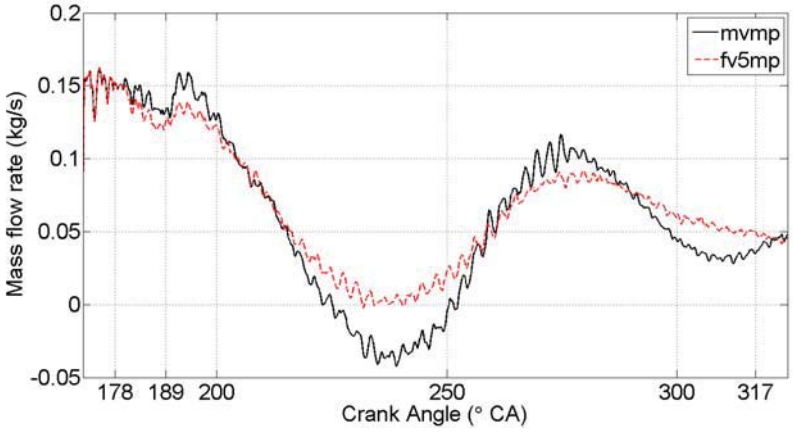

FIGURE 5.7. Mass flow (kg/s) through the exhaust valves from cylinder to exhaust port in case T1 and T2. Black curve: case T1 with moving valve and moving piston; Red curve: case T2 with fixed valve moving piston.

220 kPa. In the T4 case the considered temperature is 680 K. These two cases try to rebuild the flow filed with the simplifications of fixed valve.

As it was mentioned already, for the moving valves moving piston case within this sub-group, a back flow has been found during the simulated exhaust process. Figure 5.7 shows the mass flow rate through the exhaust valves as a function of CAD. Positive mass flow rates mean that the fluid is flowing out from the cylinder and negative values indicate the fluid is flowing in the cylinder (back-flow). As can be found, negative mass flow rates were associated with the case T1 (moving valves-moving piston) for about 25 CAD, between 225 CAD to 250 CAD.

It should be noted also that a mass conservation check has been performed by using the equation 5.1:

$$\int_{V_1} \rho_1 dV_1 - \int_t \dot{m}_{out} dt = \int_{V_2} \rho_2 dV_2 \tag{5.1}$$

where the first term on the left hand side (LHS) is the initial mass in the whole flow domain and the second term on LHS is the total mass out of the flow domain ($\dot{m}$ is negative when back flow occurs). The term on right hand side (RHS) is the final mass in the whole flow domain. For both T1 and T2 cases an equivalency has been found between the two sides of equation 5.1. This approves that the mass is conserved during the exhaust process. With this verification performed, a remaining possible source for the back-flow to occur

TABLE 5.4. Simulation cases with Engine like conditions, pulsating pressure outlet (second sub-group).

Case	Piston or inlet	Valve	Pressure outlet
E1	Moving	moving	Pulsating
E2	Moving	Fixed at 5mm	Pulsating
E3	Mass flow 0.32 kg/s	Fixed at 5mm	constant 282 kPa
E4	Stagnation pressure 430 kPa	Fixed at 5mm	constant 282 kPa

is the boundary condition used at the outlet boundary (i.e. constant pressure outlet).

5.2.3b. *Sub-group 2: pulsating pressure outlet.* Theoretically, there are two ways for a turbine to extract the energy from the exhaust flow: constant pressure turbocharging and pulse turbocharging (Baines (2005)). For constant pressure turbocharging, the manifold volume is sufficient large and the exhaust pressure is nearly constant in time. The advantage is that the turbine could work under steady conditions and at constant pressure ratio. However, in most automotive applications, pulse turbocharging is commonly used. The pressure is pulsating in the exhaust manifold.

Ideally for LES calculations, the time-dependent pressure data in the exhaust manifold prior to turbine should be provided by experiments. However, such data are not available. Fortunately, one dimensional simulation data are available for the same ICE Aghaali & Angstrom (2013) and these data are used with the simulations which are described in the following paragraphs.

There are four simulations in this sub-group as shown in Table 5.4: E1 with moving valve and moving piston, E2 with fixed valve and moving piston, E3 with fixed valve constant mass flow inlet, and E4 with fixed valve stagnation pressure inlet. In both cases E1 and E2, the piston will move along the black solid curve in Figure 5.5 from 171 CAD and 324 CAD. As for the cases investigated in the previous sub-group ("Engine-like condition"), in the case E1 the exhaust valves will move along the red solid curve in Figure 5.5. The exhaust valves are never fully closed and the minimum valve lift is 3.5 mm. For the case E2, the exhaust valves will be fixed when they reach 5mm at 178 CAD (dash line in Figure 5.5).

The boundary condition considered at the outlet is the pressure function in Figure 5.8, data obtained from one-dimensional simulations. The walls are considered at the same temperatures as described for the T1-T4 cases, see Subsection 5.2.3a. Also, as in the previous cases, the same solution has been used for initialization of each simulated cycle, see Figure 5.6. However, by contrast with the previous simulations regarding the test group, the cylinder in E1 and

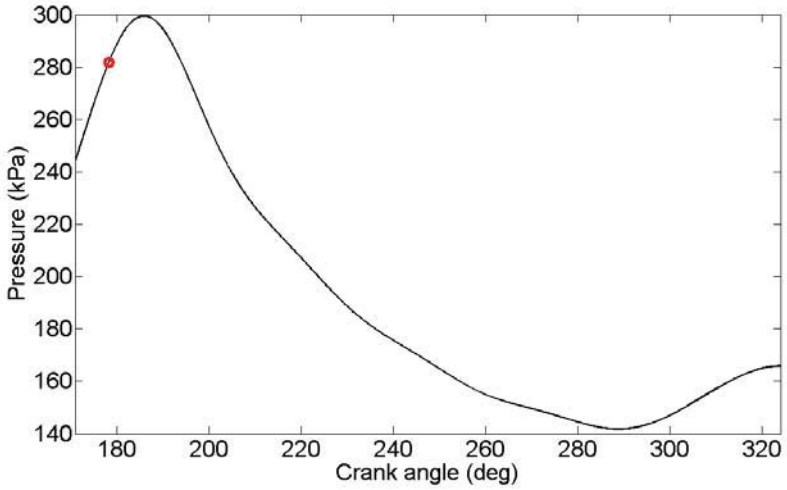

FIGURE 5.8. Pressure (kPa) outlet for simulations with Engine like condition (one dimensional simulation data from Aghaali & Angstrom (2013)). Black curve: pulse pressure outlet for case E1 and E2; Red circle: pressure outlet for cases E3 and E4.

E2 cases is "refilled" with data calculated by one dimensional simulation. Thus, the initial conditions in the in-cylinder are a stagnation pressure of 500 kPa and temperature of 1140 K for the cases E1 and E2.

Two other "simplified" setups (E3 and E4) are considered for comparisons purposes. The flow in the exhaust port is found much pulsating and dynamic with the valves and piston motion (case E1). However, some people want to rebuilt the flow field with the simplification without valves and piston motion. Here, two different cases (E3 and E4) have been set up for the trial. In the case E3, the constant inlet mass flow equals the averaged mass flow rate (0.32 kg/s) through the exhaust port calculated by in case E1 at 178 CAD (5 mm valve lift). In the case E4, the stagnation pressure inlet equals the averaged stagnation pressure (430 kPa) in the cylinder as calculated for the E1 case at 178 CAD (5mm valve lift). The inlet temperatures are the same as the average in-cylinder temperature at 178 CAD of case E1, i.e. 1090K. The pressure outlet condition considered for E3 and E4 corresponds to the 282 kPa value (at 178 CAD), marked with a red cycle in Figure 5.8. Both simplified setups cases E3 and E4 try to rebuild the flow field at 178 CAD obtained with the more complex set-up of case E1.

5.2.3c. *Sub-group 3: the whole exhaust process (on going).* As previously mentioned, this last sub-group considered as part of the "Engine-like condition" is the most complex and sophisticated one used to model the exhaust flow. It is represented by one case (E5) which considers piston motion and complete closing of the exhaust valves. The whole exhaust process from 136 CAD to 359 CAD is simulated by E5 case. The exhaust valves are fully closed at the start and at the end, during their motion. As can be found in Figure 5.5, the blue dash curves plus the red solid curve indicate the whole motion of the exhaust valves.

The boundary conditions are almost the same as those used with the simulations in second sub-group. The pulsating pressure outlet condition is imposed based on the pressure function given in Figure 2.12. The initial conditions in the cylinder at the beginning of each simulated cycle are 700 kPa (stagnation pressure) and 1240 K for the temperature.

CHAPTER 6

Results and Discussion

This chapter presents selected results from the numerical studies performed on the exhaust flow in the exhaust port of the D12, SCANIA engine. The results can be separated according to the two categories of cases already exposed in the previous chapter, i.e. results from the "Laboratory-like condition" simulations and from the "Engine-like condition" simulations.

The detailed set up of "Laboratory-like condition" flow calculations is given in Chapter 5. A grid sensitivity study has been performed for one of the "Laboratory-like condition" configurations and the outputs of the study were presented in Chapter 5 (Wang *et al.* (2013)). However, it is not sufficient to reveal that the numerical methods can compute an adequate solution to the physical problem in order to trust a particular flow solver. A direct comparison between the numerical results and experimentally measured data is always desirable. It is unfortunate that in many situations detailed comparisons between computational and experimental data cannot be performed due to several reasons (e.g. limitations with experimental techniques, requiring optical access). Regarding the present investigation, experimental data in terms of total pressure losses are available and the comparison with the LES and URANS data are detailed within Section 6.1.1. The overall characteristics of the exhaust flow in the port and the details of the flow structures are given in Section 6.1.2.

The geometrical contraction, enlargement, and pipe-bend influence on the flow losses are exposed and the responsible mechanisms are investigated. About 80% of the total pressure loss occurs in the near valve-gap region of the exhaust port. The empirical formulas presented in Chapter 2 have been used to estimate the total pressure loss generated by different mechanisms (Section 6.1.3).

Within the "Engine-like condition" simulations, the valves and/or piston motion is included in some of the cases. Within the ICE gas exchange processes, the flow losses represent a topic of major interest. The real mass flow rate is indicated by means of discharge coefficient, C_D (see also Chapter 2). However, there are no systematic studies performed in order to show how the valves and/or the piston motion affect the discharge coefficient/losses associated with the exhaust port and manifold. Usually, the discharge coefficients are obtained by performing simple experiments at fixed valve lifts and low pressure drops

on air flow benches (Danov (1997), Decker (2013)). Such predictions for the discharge coefficients cannot be very accurate due to the assumptions made. Moreover, the flow in the air flow bench tests has almost no similarity to the flow in a real working ICE. By using unsteady computational tools allowing modeling piston and exhaust valve motions, the discharge coefficients are calculated for different "Engine-like condition" set-ups (Chapter 5). The different set-ups used are representing different levels of simplicity. The discharge coefficients are calculated following the strict definition given by e.g. Heywood (1988).

6.1. "Laboratory-like condition" results

In the vehicle industry, one-dimensional simulations and three-dimensional simulations using Unsteady Reynolds Averaged Navier-Stokes (URANS) based models are widely carried out. However, both formulations are not capable of resolving the important 3D flow and vortical-scales in the exhaust port and the interaction with the walls. On the other hand, Large Eddy Simulations (LES) have the capabilities of solving accurately a large proportion of the flow scales and predict the instantaneous energy transfer. This approach is the preferred one within this study in order to assess the dynamics associated with the exhaust flow.

6.1.1. *Comparison of simulations and experiments*

The numerical solutions need to be validated against experimental measurements in order to show credibility. Table 6.1 gives a direct comparison in terms of pressure loss between the numerical results and the experimental data for three different valve lifts (i.e. 3mm, 4mm and 5mm). The computations correspond to the "Laboratory-like condition" cases L4, L5, and L6 detailed in Table 5.2(Section 5.2.1 in Chapter 5). The experiments were carried out at SCANIA. A total pressure drop of 4.9 kPa was imposed between the engine's cylinder and the exit of the outlet pipe during the experimental flow bench tests. The experiments (air flow bench tests) were run for the 3mm, 4mm and 5mm valve lifts, respectively and the mass flow rates through the exhaust port were measured. The measured mass flow rate data can be found in Table 5.2 (Section 5.2.1 in Chapter 5) for the three different valve lifts (L4, L5, and L6 cases). During both LES and URANS simulations the mass flow rates were imposed as boundary conditions and the pressure drop values were calculated between the in-cylinder (i.e. the cross plane "in" in Figure 2.3) and the exit of the exhaust port (i.e. the cross plane y=10d in Figure 2.3). Note that the URANS calculations (preferred computational tool by industry) were performed for comparison purposes.

TABLE 6.1. Total pressure loss (kPa) obtained experimentally is compared against results obtained using URANS and LES.

Valve lift	URANS	LES	Experiments
3mm	5.4	5.0	4.9
4mm	5.4	4.9	4.9
5mm	5.3	4.8	4.9

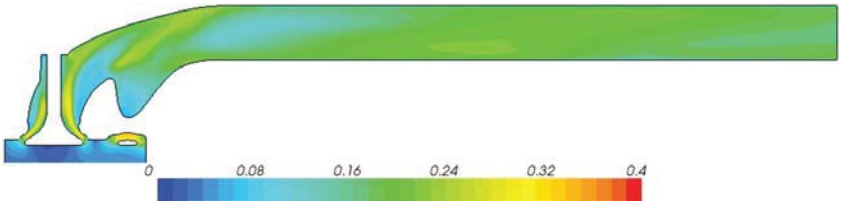

FIGURE 6.1. Time averaged Mach number as calculated by LES in a longitudinal plane cutting one of the exhaust port and the exit pipe, case L6.

As can be found in Table 6.1, LES predicts the pressure loss in a close agreement with the experimental data (differences within 2%). The estimations for the total pressure loss using the URANS approach are slightly overestimated (differences roughly within 10%) compared to the values obtained by LES and the experiments. Given being the complex nature of the flow in the exhaust port (Section 6.1.2) characterized by flow separation, induced shear-layers, and stagnation regions this is not unexpected.

6.1.2. *Flow characteristics and associated pressure losses*

The general flow structures in the exhaust port are described using the LES data obtained for a 5mm valve lift, i.e. case L6 in Table 5.2. The maximum Mach number is about 0.3, value reached in the gap region between the exhaust valve and its seat, see Figure 6.1. Hence, for the laboratory-like conditions, the flow can be theoretically thought as being a low-Mach number flow, i.e. incompressible. This assumption is however not considered within the present compressible calculations.

Considering the instantaneous velocity filed in the exhaust port and manifold (Figure 6.2) one can distinguish that the flow is highly unsteady, turbulent with a wide range of vortical-scales and large velocity gradients in the radial direction just downstream of the exhaust gap region in the exhaust port. The largest scales are on the order of exhaust pipe diameter (integral length scale). The smallest scales resolved are about the size of the computational grid. The

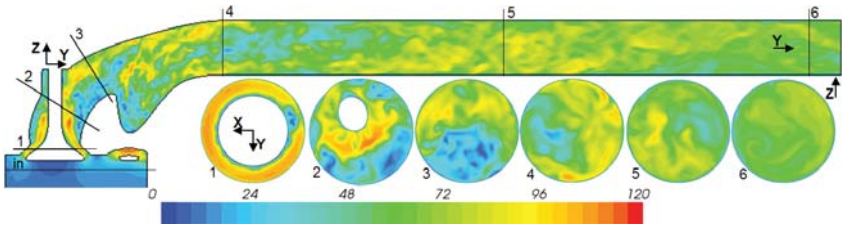

FIGURE 6.2. Instantaneous velocity magnitude (m/s) in the exhaust port and manifold as calculated by LES for a 5mm valve lift, case L6, Laboratory-like conditions.

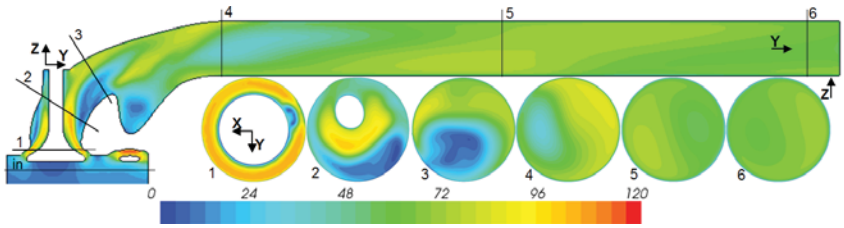

FIGURE 6.3. Time averaged velocity magnitude (m/s) as calculated using LES for the case L6.

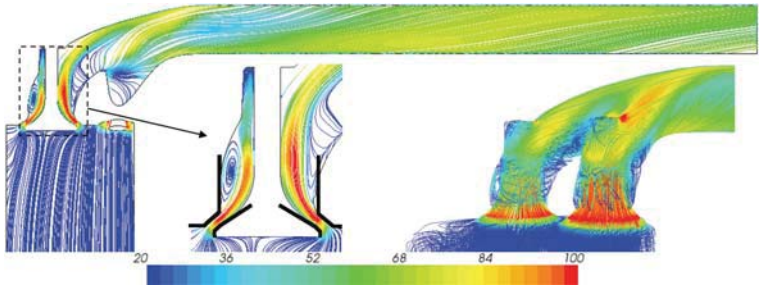

FIGURE 6.4. Streamline distribution in the flow field of case L6. Streamlines in a longitudinal plane showing the recirculation of the flow in the exhaust port and three dimensional streamlines distribution in the exhaust port. The streamlines are colored by time averaged velocity magnitude (m/s).

PSD plots show that the resolution of the computational grid employed was sufficient to solve about an order of magnitude of the inertial sub-range (see Figure 5.4), which includes the Taylor micro-scale (Pope (2000)).

Figure 6.3 shows the time-averaged LES data based velocity magnitude distribution in a longitudinal plane and several cross-sectional planes cutting

the exhaust port 4b and the exit manifold (see Figure 2.3 for the notation used) . The flow goes through the valve's gap from the cylinder towards the exit pipe. Due to the geometrical contraction, the flow is initially accelerated with a peak velocity of about 110 m/s in the valve gap. Note that because of the idealized, Laboratory-like conditions, this velocity is very low as compared with a real case scenario. This will be further discussed when the "Engine-like condition" configurations will be analyzed. Controlled by the valve's contour and the shape of the port, an annular, high velocity, unsteady, jet-like flow structure is generated in the near gap area. Passing the valve gap, the flow expands into the exhaust port and decelerates since the cross sectional area increases. However, the jet like flow still has a large velocity, strong velocity gradients being observable in the valve's radial direction as the flow follows the valve stem. Due to the sudden expansion, flow separation and recirculation regions are found in the exhaust port, see Figure 6.4. When the high velocity jet like flow arrives at the top of the stem, it impinges on the wall of the manifold and is bended along the curvature of the exhaust port. There are two passages joined into the exit manifold pipe, one coming from each of the exhaust valves (4a and 4b in Figure 2.3). Similar flow behavior and structures are found in both conduits and there is an important interaction between the two streams coming from the two exhaust valves within the exit pipe. Visualizing the low velocity flow region downstream of the merging point of the two passages, see Figure 6.3 and Figure 6.4), it is observed that a secondary helical flow structure is generated in the exit pipe.

With the purpose of illustrating where the main total pressure loss occurs, the whole flow domain has been divided into several segments and for each of them the total pressure losses were calculated. In the Table 6.2 the second column (P_{tot}), area weighted time averaged pressure values calculated based on the LES data are presented along several cross planes. The locations of each cross planes are shown from in-cylinder location (*in*) to plane 6 in Figure 6.3. The total pressure loss between the cross-plane *in* and the cross-plane 6 is 4.8 kPa, representing the whole (100%) total pressure loss. It is found that the pressure loss between the *in* cross-plane and cross-plane 2 is 3.6 kPa, which represents 75% of the total.

The same observation was found when analyzing the URANS data corresponding to the same L6 "Laboratory-like condition" case, see Table 6.3. In the URANS case a 77.4% of the pressure losses occur between the cross-plane *in* and cross-plane 2 (see Figure 6.3 for the locations of the cross planes).

It is interesting to note that in the LES results the total pressure loss from cross-planes 1 to 2 is higher (47.9%) than the value obtained by using the cross-plane *in* and cross-plane 1 (27.1%). On the opposite, URANS predicts a higher total pressure loss between cross-plane *in* and cross-plane 1. We will get back

TABLE 6.2. Total pressure loss (kPa) of LES results at different cross-planes, at 5mm valve lift, L6 case, Laboratory-like condition.

Cross plane	P_{tot}	ΔP_{tot}	Percentage
in	108.6	-	-
1	107.3	1.3	27.1%
2	105.0	2.3	47.9%
3	104.5	0.5	10.4%
4	104.0	0.5	10.4%
5	103.9	0.1	2.1%
6	103.8	0.1	2.1%

TABLE 6.3. Total pressure loss (kPa) of URANS results at different cross-planes, at 5mm valve lift, L6 case, Laboratory-like condition.

Cross plane	P_{tot}	ΔP_{tot}	Percentage
in	108.9	-	-
1	105.7	3.2	60.4%
2	104.8	0.9	17.0%
3	104.6	0.2	3.8%
4	104.2	0.4	7.4%
5	103.9	0.3	5.7%
6	103.6	0.3	5.7%

to this observation when the data based on the empirical formula estimations will be discussed (Section 6.1.3).

6.1.3. *Pressure losses: empirical formula estimations*

There are several mechanisms which can cause total pressure losses in a pipe system, for example Expansion, Friction, Bends. In applied fluid mechanics, empirical formulas are often used for the estimations of the total pressure losses due to different mechanisms, see Chapter 2. Under "Laboratory-like condition", the flow Mach number is small enough (bellow 0.3), see also Figure 6.1, and the density of the air does not change considerably (cold flow). Under such and additional other assumptions (e.g. no heat transfer, no mechanical devices would add energy or remove energy between the two sections of interest), empirical formulas can be used. One can keep in mind that given the complexity of the geometry in the exhaust port, it is really not reliable to use these formulas to

get accurate values of the total pressure losses. It is reasonable to use these formulas to calculate only as an estimation of the pressure loss values.

6.1.3a. *Total pressure losses generated by geometrical contraction.* Geometrical contraction is encountered by the flow is the fluid from the cylinder enters the gap with a 90° cone angle (shaped by the cylinder head, exhaust port and valve edge in Figure 6.4. Figure 6.4 shows that when the streamlines approach the gap, they are curved forming a "vena contracta" with a minimum flow area occurring in the gap. The turbulence caused downstream from the initial contraction and the subsequent expansion generates the energy loss (Robert (2005)). The total pressure loss due to this gradual contraction can be calculated by equation (2.14),

The resistance coefficient, K_c, depends on the diameter (or area) ratio and cone angle. The area ratio between cross-plane *in* and cross-plane 1 (see Figure 6.3) is 24. There are two port channels, so the area ratio is 12 for the gradual contraction and then the diameter ratio is 3.5. By checking the resistant coefficient diagram for gradual contraction in Figure 2.7 for a diameter ratio greater than 3, one can find the resistant coefficient of about 0.19 for a 90° cone angle. Assuming incompressibility (based on the low Mach number flow) the air density is assumed to be constant at 1.20 kg/m^3. From Figure 6.3 and Figure 6.4, the velocity V_{gap} is considered at 110 m/s.

Hence, the total pressure loss calculated by equation (2.14) is 1.4 kPa. Compared to the LES data based total pressure loss listed for the near-gap region of the valve (Table 6.2), it is a good estimation. Hence, the total pressure loss generated by the gradual contraction is on the order of thousands (Pascal).

6.1.3b. *Total pressure losses generated by geometrical expansion.* When the fluid flows out of the gap to the exhaust port, it is exposed to a geometrical expansion. The expansion region is bounded by the valve top surface and the surrounding walls of the exhaust port, see Figure 6.4. The bend effect of the exhaust port is neglected in this estimation process for expansion and will be counted separately whereas in next sub-section the corresponding loss in the pipe bend is considered. The expansion is simplified by assuming straight walls in the exhaust port (black lines in Figure 6.4) with a 45° cone angle. The total pressure loss generated by this gradual expansion can be estimated by equation (2.15).

The resistance coefficient of gradual expansion, K_e, depends on the diameter (area) ratio and the cone angle. The area ratio is 8/5 between the cross-plane 2 and cross-plane 1. Hence the diameter ratio is 1.26. Checking on the resistance coefficient in Figure 2.9 and Tables (see e.g. Robert (2005)), it is found that K_e is between 0.4 and 0.47. Hence, the total pressure loss caused by the gradual expansion is about 2.9kPa to 3.4kPa. This is on the

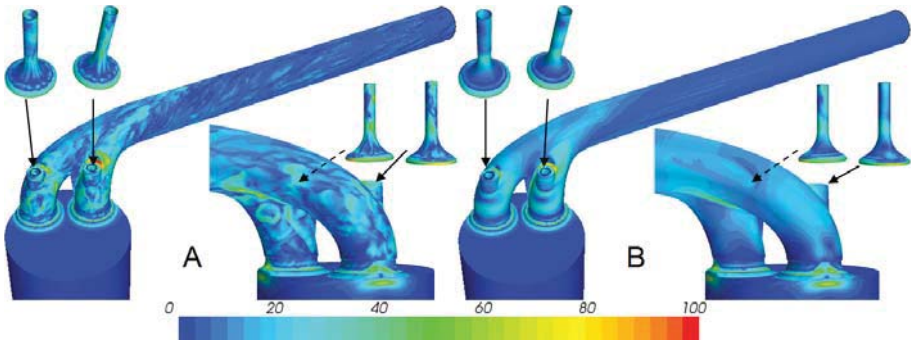

FIGURE 6.5. Wall shear stress distribution (Pa) in the exhaust port and manifold, LES simulation of case L6. A: Instantaneous wall shear stress distribution; B: Time-averaged wall shear stress distribution.

same order of magnitude as the total pressure loss listed in Table 6.2 (based on LES data), between the cross-plane 1 and cross-plane 2. Note that differences were expected between the empirical obtained data and the CFD.

6.1.3c. *Total pressure losses generated by a pipe bend.* The total pressure losses for the bended exhaust port can be calculated by equation (2.16). The loss coefficient for the bend (k_b) depends on the bend angle and the ratio between centerline radius of the bend and the internal diameter of the pipe. The bend angle is assumed to be 90°, see Figure 6.4. The centerline radius of the bend, following the entire geometry from the cylinder head to the centerline of the exit pipe, was measured as 75 mm. The internal diameter is assumed to be the diameter of the exit pipe (42 mm). Thus, the ratio of the centerline radius of the bend and the internal diameter of the pipe is approximately 1.78. The loss coefficient K_b can be estimated as being between 0.24 and 0.3 from the Figure 2.11. Velocity v is time averaged velocity in the bend of the exhaust port. The area weighted velocity in the cross-plane 3 is employed here (45 m/s). Then the total pressure loss caused by the bend exhaust port can be estimated as being between 0.3 kPa and 0.4 kPa, which is on the order of hundreds of Pascal.

6.1.3d. *Total pressure losses due to friction.* When the fluid flows in the exhaust port and the exit pipe, molecular diffusion causes momentum exchange between layers of the fluid, which are moving at different velocities. The net result is exhibited in the shear stresses between adjacent layers of the fluid. In the presence of the side walls, wall shear stresses (WSS) occur. To counter balance the WSS, a pressure loss occurs in the fluid. In CFD simulations, WSS values have been calculated at all the solid surfaces in the computational domain. Figure 6.5 shows the instantaneous and time averaged wall shear stress

TABLE 6.4. Total pressure loss (kPa) estimated by empirical formulas of different mechanisms, case L6, Laboratory-like condition.

Mechanisms	ΔP_{tot}	Positions
Contraction	1.4	from cross plane "in" to cross plane 1
Enlargement	2.9-3.4	from cross plane 1 to cross plane 2 or 3
Bend	0.4	from cross plane 1 to cross plane 4
Friction 1	0.3	from cross plane "in" to cross plane 4
Friction 2	0.2	from cross plane 4 to outlet

distribution in the exhaust port and exit pipe. With the calculated wall shear stress values, the total pressure loss caused by friction forces can be calculated. See the relation equation (2.11) for the friction forces.

The wall-shear stress (τ_w) acting on the wall area segment (A_{wall}) are considered. Once the friction forces are calculated, the pressure drop generated by friction can be estimated, (equation 2.13). The calculations have been taken in two separated parts: the exhaust port (which includes the valves) and the exit pipe. The friction loss at the cylinder wall is considered very small and neglected. The effective area ($A_{eff.}$) of the bulk flow in the exit pipe is easy to get from the area of the cross-plane 4 (in Figure 6.3). In the exhaust port, due to the irregular shape of the port and the existence of the valve, it is really difficult to get the accurate effective area ($A_{eff.}$) for the exhaust port. The value used is an average of several cross planes of the exhaust port. The calculated results are 0.2 kPa for the exit pipe and 0.3 kPa for the exhaust port. Thus, the total pressure losses due to friction are on the order of hundreds (Pascal). By analyzing this together with the LES total pressure losses listed in Table 6.2, one can deduce that the friction loss in the exhaust port cannot be the dominate mechanism for losses in the exhaust port. However, it may be an important mechanism for losses in the exit pipe.

The total pressure loss generated by different mechanisms as estimated using empirical formula can be summarized in Table 6.4. For the considered Laboratory-like condition, when comparing the estimations based on empirical formulas against the LES based data presented in Table 6.2, one can observe that there are differences but not very significant. In other words it makes sense to use empirical formulas for estimating total pressure losses under Laboratory-like conditions.

The total pressure losses are dominated by the contraction and expansion. Energy is loss through vortex enhanced energy dissipation, flow separation and induced secondary flow motion.

An interesting observation is that the empirical formula estimations disagree somehow with the URANS calculations. The URANS results (Table 6.3) show that the largest total pressure loss occurs between cross-plane *in* and cross-plane 1. Based on the LES data and the empirical formula estimations, the largest total pressure loss occurs between cross-plane 1 and cross-plane 2 and is generated by the expansion.

URANS (k-epsilon) simulation cannot capture the total pressure loss associated with the flow behavior in the expansion region, since cannot handle properly the flow anisotropy (e.g. adverse pressure gradients, separated flow, induced secondary flow motion). Compared to URANS, LES should be the preferred approach to be used in order to accurately describe the behavior of the flow in such a complex 3D geometry, which involves asymmetric curved passages and sudden changes in the cross-sectional area.

6.2. "Engine-like condition" results

In industry, the discharge coefficients of exhaust ports are often estimated based on flow measurements on air flow benches. There are some important assumptions made and simplifications considered with such tests, some of which are quite severe. Within the air flow bench tests, the pressure difference between the in-cylinder and exhaust port is small (2.5 to 7 kPa). However, the real pressure difference in an engine-like condition can be over 500 kPa. The temperature effect is not considered, the flow being "cold". In reality, the temperature can be over 1000 K. Maybe, the most important simplification with the air test benches is that the flow dynamics due to the motion of the piston and valves are neglected, the valves being fixed at a certain valve lift. Under realistic conditions, the movement of piston could generate strong pulses and the valve motion modulates the flow exhausting the cylinder.

This section presents some of the major differences in terms of the flow field and flow losses when considering more realistic set-ups then the Laboratory-like set-ups.

6.2.1. *Discharge coefficients*

Discharge coefficients have been calculated for four simulations (Sub-group 2) under "Engine-like condition". Following the strict definition in equation 2.21 to equation 2.23, p_0 is the area weighted stagnation pressure monitored at the cross plane "in" (see Figure 2.3). T_0 is the area weighted stagnation temperature at cross plane "in".

There are two exhaust valves corresponding to each of the cylinders (valve 2 and valve 3 in Figure 2.3). Thus, the mass flow rates are measured separately for each valve just at their gap position, as well as the static pressures. The

data used for the calculation have been phase-averaged over ten cycles in cases E1 and E2.

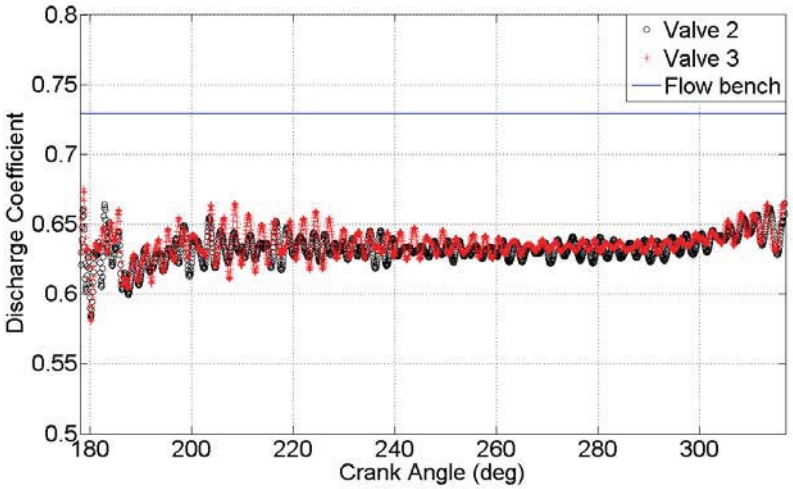

FIGURE 6.6. Discharge coefficients of valve 2 and valve 3 in case E2, from 178 CAD to 317 CAD.

Figure 6.6 shows the discharge coefficients in case E2 calculated for the two exhaust valves (denoted by 2 and 3 in Figure 2.3). This case considers the valves fixed at 5mm valve lift from crank angle 178 CAD to 317 CAD and the motion of the piston according to Figure 5.5. The discharge coefficients for both valves are showing some oscillations when plotted as a function of crank shaft angle degree. The minimum value is about 0.58 at 180 CAD and the maximum value is about 0.69 in 317 CAD. Another observation is that the magnitude of the fluctuations is a function of CAD. Thus, from about 240 CAD to 300 CAD, the magnitude of the fluctuations are relatively low as compared with the rest of the cycle.

In average, the discharge coefficients for both valves are nearly the same, see Figure 6.6. The same conclusion can also be found when analyzing cases E3 and E4, which do not consider the motion of the piston and the pulsating pressure conditions at the outlet. Thus, the discharge coefficients calculated for Case E3 are of 0.617 for valve 2 and 0.619 for valve 3. The difference is 0.3 %. In the case E4, the discharge coefficients are 0.621 for valve 2 and 0.623 for valve 3. The difference is also within 0.3%.

Commonly with the air flow bench tests, the static pressure just at the valve gap is not measured directly (difficult access due to the complex geometry). Instead, a total pressure drop of known value is imposed (Section 2.2.7). By

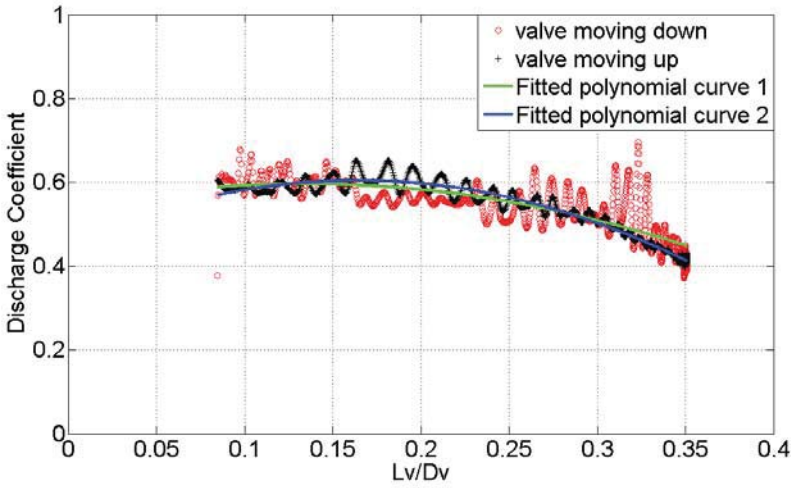

FIGURE 6.7. Discharge coefficients in case E1, with valve and piston motion. Red circle: valves moving dwon; Black plus: valves moving up.)

simulating such Laboratory-like conditions, e.g. case L6 for a fixed 5mm valve lift, it was found that the discharge coefficient of case L6 is 0.714. This value is very different from the values calculated for the E2, E3, and E4 cases. The maximum difference can reach 20% when referring to the discharge coefficients calculated for the E2 condition (see Figure 6.6).

The motion of both piston and valves is considered in the case E1. Thus, from 171 CAD to 247 CAD, the valves move down from a valve lift of 3.5 mm to the maximum valve lift (14 mm), and then they move back from 248 CAD to 324 CAD. Figure 6.7 shows the discharge coefficients as a function of normalized valve lift, when considering piston and valves motion (E1 case). It has been found that the discharge coefficients of valve 2 and valve 3 are almost the same. Therefore, only the discharge coefficients of valve 2 are plotted, when valve moves towards maximum valve lift (valve moving down) and when valve moves back. The red circles represent discharge coefficients when the valve 2 is moving down, and the black crosses indicate the values of the discharge coefficients as the valve 2 moves up. In Figure 6.7, there are also two fitted polynomial curves for the discharge coefficients of moving down phase (green curve) and moving up phase (blue curve). Both in the moving down phase and moving up phase, the discharge coefficients are pulsating. However, the general trend is that the discharge coefficients decrease at large valve lifts.

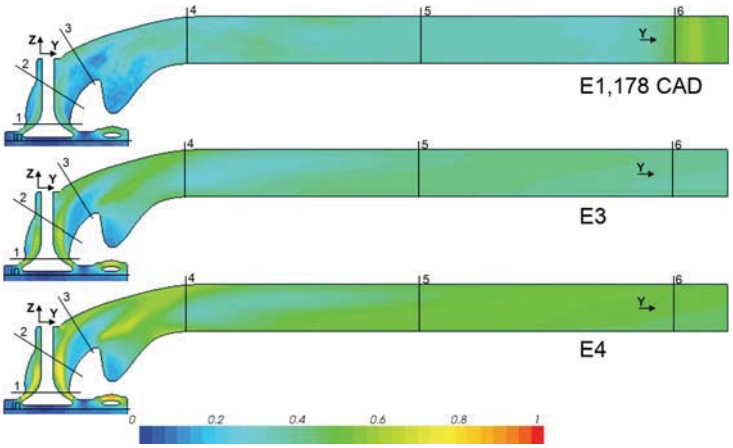

FIGURE 6.8. Mach number comparison between cases E1 (178 CAD), E3 and E4. From top to bottom: Phase averaged Mach number distribution in case E1; Time averaged Mach number distribution in case E3; Time averaged Mach number distribution in case E4.)

6.2.2. *Comparisons between E1, E3 and E4 cases*

Cases E3 and E4 (without piston and valve motion) were considered in order to reconstruct the flow field at 178 CAD of the E1 case (which considers the motion of piston and valves). Note that at 178 CAD the valve lift is at 5 mm for the E1. The detailed justification, setup, and boundary conditions can be found in Section 5.2.3b.

Figure 6.8 shows the Mach number distributions in the exhaust port and pipe for case E1 at 178 CAD, case E3, and case E4, respectively. In all these cases, the maximum Mach numbers are all smaller than 1. However, they are quite different in values. In case E4, the maximum Mach number is 0.9 at the gap position. In case E3, the maximum number is 0.7 at the gap. There is a qualitative agreement between the Mach number distributions calculated for the static configurations, cases E3 and E4. The pulses caused by the motion of the piston and the flow modulation imposed by the valve (case E1), changes completely the flow configuration for the particular instance of 178 CAD. In this case the maximum Mach number based on phase-averaged data is only about 0.5.

Figure 6.9 shows comparison of velocity fields between the three different cases. It can be found that the velocity magnitudes in case E1 at 178 CAD are much smaller than the other two cases. The velocity distribution is quite different from the other two cases. The velocity magnitude at cross plane 6 is

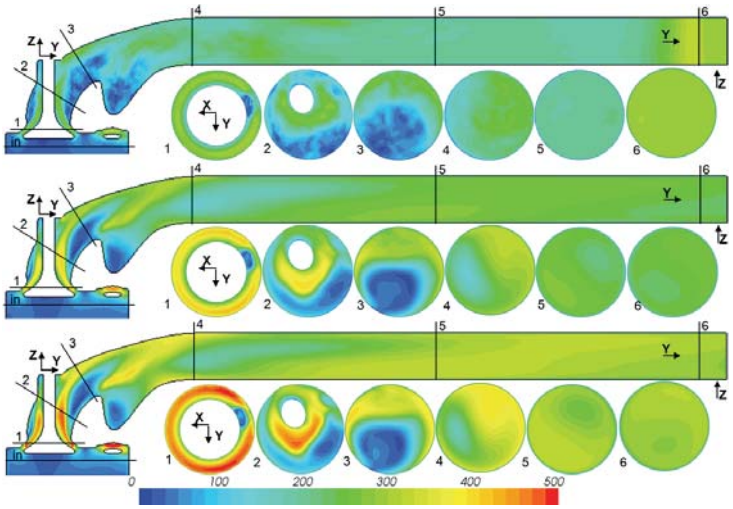

FIGURE 6.9. Velocity magnitude (m/s) comparison between cases E1 (178 CAD), E3 and E4. From top to bottom: Phase averaged velocity distribution in case E1; Time averaged velocity distribution in case E3; Time averaged velocity distribution in case E4.)

higher than the velocity at cross planes 2, 3, 4 and 5. From an animation of the flow development, one can find that the high velocity region corresponds to the initial pulse from the beginning of the cycle when the valve lift is of 3.5 mm.

The flow in the exhaust port is dynamic and developing with the piston and valve motion in case E1. This dynamic process is totally changed with the steady inlet flow with fixed valves (cases E3 and E4). This is despite of the fact that the inlet boundary conditions employed in the E3 and E4 cases are reproducing the in-cylinder mass flow condition and respectively the in-cylinder stagnation pressure which corresponds to the 178 CAD for case E1.

Figure 6.10 shows the total pressure distribution in the three cases: E1 at 178 CAD, E3 and E4. Total pressure distribution in case E1 at 178 CAD has no similarity with the other two simulations. It has been found that area weighted phase averaged total pressure of cross plane 5 is higher than the area weighted phase averaged total pressure of cross plane 4 in E1 at 178 CAD. This phenomenon cannot be found in cases E3 and E4. From this analysis one can conclude that the associated total pressure losses cannot be predicted accurately without considering the valves and piston motion.

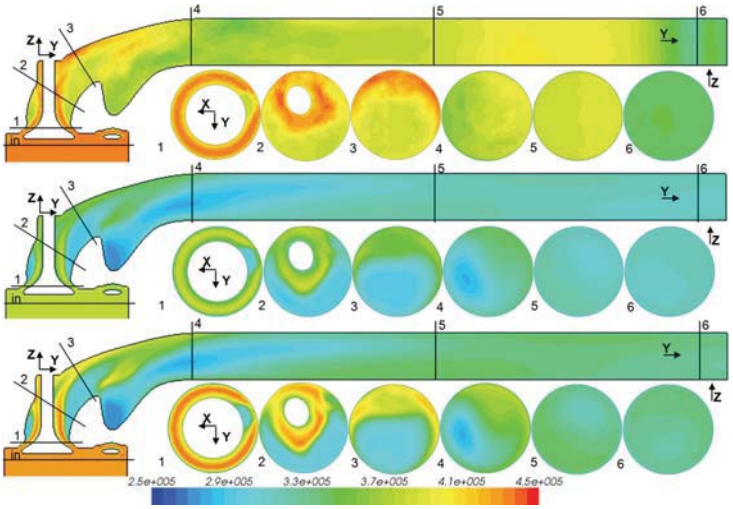

FIGURE 6.10. Total pressure (Pa) comparison between cases E1 (178 CAD), E3 and E4. From top to bottom: Phase averaged total pressure distribution in case E1; Time averaged total pressure distribution in case E3; Time averaged total pressure distribution in case E4.)

6.2.3. *Towards predicting a complete exhaust process; case E5*

Case E5 represents an initiative of simulating the whole exhaust process from 136 CAD to 359 CAD, see Section 5.2.3c. The simulations are still on-going. Figure 6.11 shows the instantaneous velocity field at different CAD. In the initialization at 136 CAD of each cycle, the cylinder will be "refilled" imposing a high pressure (700 kPa) and high temperature (1240 K) air initially stagnant. On the other hand, the flow variables in the exhaust port are kept from the previous cycle calculated at the time instance of 359 CAD (see the initialization process described in Section 5.2.3a). Hence, at 137 CAD, there is residual flow in the exhaust port even though the valves are closed. The maximum velocity is about 56 m/s.

At 150 CAD, the valve lift is 0.67 mm. The flow is found to impinge on the exhaust valve stem. The maximum velocity can reach values as high as 800 m/s. At 175 CAD, the valve lift is at about 4.3 mm. The high velocity and high temperature gases fill in already the exhaust port region. The maximum velocity is in the valve gap region (about 560 m/s). At 205 CAD, the exhaust valve lift increases to 10.69 mm. The maximum velocity is about 140 m/s. However, the location of the maximum velocity is not at the valve gap but at the junction between the two exhaust ports (y=0d in Figure 2.3). The

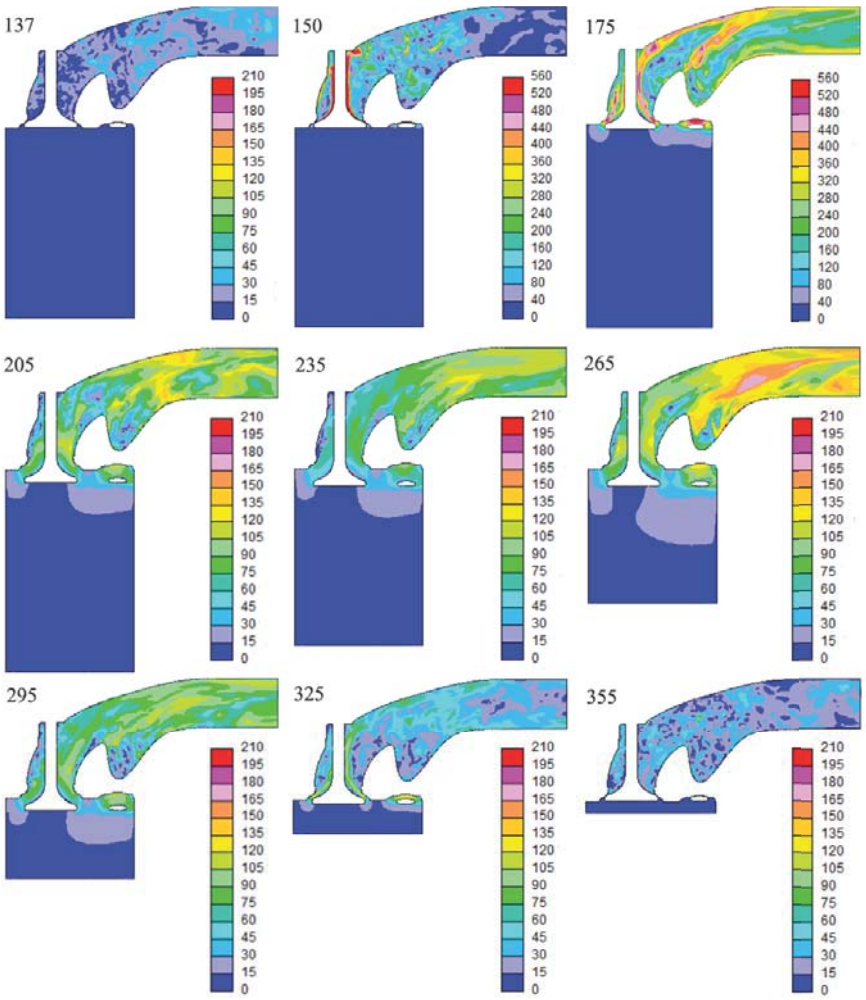

FIGURE 6.11. Instantaneous flow field with velocity magnitude (m/s) distribution in different crank angles degrees (top left corner in each sub-figure), case E5 with the whole exhaust process.

same phenomenon can be also found at 235 CAD, 265 CAD, and 295 CAD. The reason is that the contraction of two exhaust ports turning to one exit pipe. The total cross-sectional area section is minimal at the location of the junction (y=0d in Figure 2.3) and not in the region of the exhaust valve's gap. Moreover the piston moving towards the TDC accelerate the gases into the exhaust manifold. At 325 CAD the valves moves towards closing, the valve

lift being about 3.3 mm. Most of the residual gases have been exhausted. The velocity is not so high as in the 145 CAD and 175 CAD instances. At 355 CAD, the valve lift is close to zero (0.09 mm), the valve separating the cylinder from the exhaust manifold. As a general observation, the exhaust process is very dynamic. The ratio of maximum velocities for different CAD can be as high as 15. For small valve lifts (0.67 - 4.3 mm), the maximum velocity occurs at the valves gap. However, at large valve lifts (over 10 mm) during the scavenging phase, the maximum velocity is found at the junction position in the exhaust pipe.

CHAPTER 7

Summary and Future Work

Large Eddy Simulation calculations of the unsteady compressible exhaust flow associated with an ICE have been carried out under Laboratory-like and Engine-like conditions, respectively. URANS calculations were considered for a very limited number of cases only for comparison purposes. The main reason for the research was to quantify the losses associated with the flow in the exhaust port and manifold and investigate the responsible mechanisms. In the same time, it is important to assess the limitations associated with the Laboratory-like condition situations.

In the "Laboratory-like condition" simulations, valves are fixed at certain valve lifts of interest, i.e. 3mm, 4mm, and 5mm for which experimental data exists. Thus, proper boundary conditions are chosen to match the experimental set up at SCANIA. Only "cold" flow calculations are performed during this phase. Engine-like condition calculations considered the temperature effect. Some cases included the valve or piston motion, while some other (simplified) were run in order to replicate the flow filed in a working engine with simplifications related to the valve and piston motion.

7.1. "Laboratory-like condition" simulations

LES and URANS (standard $k - \epsilon$) flow calculations has been performed in order to quantify the flow field and the losses associated with the exhaust port geometry of a heavy duty Diesel engine. Thus, air flow bench tests performed at SCANIA are replicated by using CFD. The calculations were carried out for three different exhaust valve lifts. The comparisons between the LES, URANS, and existent experimental data in terms of the total pressure loss suggested that the LES should be the preferred approach to be used in order to be able to describe the dynamics and the behavior of the flow in the very complex 3D geometry. This is even more important when considering the pulsatile flow in the engine exhaust port since as the flow is far from being fully developed homogeneous, isotropic (class book) turbulence. The flow is transitional and therefore the length scale spectrum is limited. Therefore, LES can capture most, if not the whole spectrum, even if the same grid is not adequate for resolving a corresponding continuous flow situation. Geometrical complexity

stems from the presence of valves, and the asymmetric curved passages with sudden changes in the cross-sectional area. These geometrical aspects generate unsteady large scale structures that are captured well by LES.

It was found that unsteady, relatively large vortical scales dominate the flow in the exhaust port. About 80% of the total pressure loss occurs in the near gap region of the exhaust valve and comes from the contraction and the enlargement process of the flow. The energy dissipated through flow separation and induced secondary flow motion is the main source for the total pressure losses.

Possibly, a way of reducing the total pressure losses associated with the exhaust port would be to optimize the geometry of the exhaust port in order to avoid corners, sharp turns of the flow or flow separation.

7.2. "Engine-like condition" simulations

Engine like simulations were designed to evaluate the effect of valve motion and piston motion to the flow in the exhaust port. Focusing on the flow losses through the exhaust valves, discharge coefficients haven been calculated for all the simulations in sub-group 2 under "Engine-like condition", see section 5.2.3b. It has been found the discharge coefficients of the two valves in the exhaust port (as discussed for Valves 2 and 3 in Figure 2.3) are nearly the same even with valves or piston motion. Small differences (within 0.3%) were observed (Cases E2, E3, and E4).

The flow through the exhaust port has been found fluctuating for valve or piston motion (Case E1). Hence, the discharge coefficients in the different sections are also time-dependent. The discharge coefficients obtained based on the air flow bench tests could be as large as 20% as compared with the hot flow cases which include the piston motion. Advanced methods able to capture the dynamics and the fluctuations in the flow (LES) should be employed for the calculations of discharge coefficients under working engine-like situation. In this thesis, the discharge coefficients are given with the valve and piston motion for Case E1.

The simplified Cases E3 and E4 failed to capture the flow field calculated in Case E1 at 178 CAD. Note that a limited number of cycles were used for calculating the phase-averaged flow data presented for Case E1. Nevertheless, this result indicates that the effect of valves and piston motion cannot be neglected.

Thus, it is necessary to do study and analyze the details and dynamics of the flow with valves and piston motion. LES is be best method for such studies. However, it has been found that the issue of imposing appropriate boundary conditions is a very important issue for LES.. Therefore, understanding the

details of the flow and experiments play a crucial role for being able to employ appropriate boundary conditions.

7.3. Proposed future work

A combined experimental and LES studies are necessary for the analysis and understanding of the details of the flow and associate losses in the exhaust port of a working internal combustion engine.

The experimental measurements could, by visualization resolve the large scale structures, whereas optical measuring techniques (i.e. PIV and LDV) could provide at least mean and rms values for the boundary conditions. High speed PIV do not have the required temporal resolution, as yet, to provide directly all the data needed for LES. Some PIV data in the cylinder or in the exit pipe could be also obtained, see e.g. Baum *et al.* (2013*a*),Baum *et al.* (2013*b*), Peterson *et al.* (2013). Such data could be of use in validating the LES results.

The quality of LES would improve as the resolution would improve. The need for improved SGS near the walls, may be needed for situations where the wall boundary layer becoming important. Today, no rationally derived SGS for the near wall region exist. Otherwise, the need for SGS is less important for transient flows that do not allow for small scales and the energy cascade to develop. Handling the full engine exhaust port with adequate resolution should be the main goal for the future. Such study would be beneficial not only for understanding losses in the exhaust manifold, but also for improving the inlet conditions for the turbine of the turbo-charger.

CHAPTER 8

Papers Summary and Authors Contributions

Paper 1

LES of the Exhaust Flow in a Heavy-duty Engine.
O. Bodin, Y. Wang, M. Mihaescu & L. Fuchs.
LES4ICE, November 2012.
Published in Oil & Gas Science and Technology - Rev. IFP Energies nouvelles, pp.1-12 , DOI: 10.2516/ogst/2013117, 2013.

The flow in a heavy-duty engine exhaust port and manifold was investigated. The work was performed in part by Bodin (manifold) and Wang (port) under supervision of Mihaescu and Fuchs. In the exhaust port, the valve lift is fixed at 4mm valve lift. The used computational grid was supplied by SCANIA (see section 5.2.2). The paper was written by Bodin and Wang together and revised by Mihaescu and Fuchs. The work was presented at LES4ICE conference, November 29-30, Paris France. The paper was accepted for publication in Journal of Oil & Gas Science and Technology - Rev. IFP Energies nouvelles.

Paper 2

Flow Structures and Losses in the Exhaust Port of an Internal Combustion Engine.
Y. Wang & B. Semlitsch & M. Mihaescu & L. Fuchs .
Peer-reviewed and accepted paper (IMECE2013-64610) in the proceedings of the ASME 2013 International Mechanical Engineering Congress & Exposition, November 13-21, 2013, San Diego, California, USA.

The purpose of this paper is to characterize the flow around the exhaust valves (4mm) and in the exhaust port. Three computational meshes were generated with three different levels of resolution. A grid sensitivity study was carried out. Numerical solutions were compared with the available experimental data from SCANIA. The flow field was characterized and quantified for the 4mm valve lift. The associate total pressure losses were analyzed and compared with the empirical formula estimations. The major source of the total pressure loss was found in the exhaust port. The simulations were run by Wang under

supervision by Mihaescu and Fuchs. The data were processed by Wang and analyzed by Wang and Mihaescu. The paper writing was performed by Wang and revised by Semlitsch, Mihaescu and Fuchs. The paper was accepted by the proceedings of the ASME 2013 International Mechanical Engineering Congress & Exposition. Both the reviewers thought that the work was excellent and the paper was of Journal quality. Hence, the paper is to be submitted to the ASME Journal of Fluids Engineering.

Paper 3

Flow-structures Generated by Valve and Piston Motion in an Exhaust Port of a Truck Engine.
Y. Wang & B. Semlitsch & M. Mihaescu & L. Fuchs .
Published in the 4th International Conference on Jets, Wakes and Separated Flows, ICJWSF2013,September 17-21, 2013, Nagoya, Japan.

The purpose of this paper is to study the impact of dynamic valve motion or piston motion on the flow and the losses in an ICE exhaust port. The corresponding cases are the test group Engine-like condition (as described in Section 5.2.3a). The work was performed by Wang supervised by Mihaescu and Fuchs. The paper writing was performed by Wang and Semlitsch together and revised by Mihaescu and Fuchs. The paper is part of the Proceedings of the 4th International Conference on Jets, Wakes and Separated Flows-IV, Nagoya, September 2013.

Paper 4

Flow Losses under Laboratory-like and Engine-like conditions in the Exhaust Port of a Diesel Combustion Engine.
Y. Wang & B. Semlitsch & M. Mihaescu & L. Fuchs .
Manuscript to be submitted for journal publication

The purpose of this paper is to study the flow losses in both Laboratory-like and Engine-like conditions in the exhaust port of an internal combustion engine. Total pressure losses are analyzed using empirical formula estimations. The vortex distribution, turbulence kinetic energy and turbulence dissipation rate are also examined. In the Engine-like simulations, discharge coefficients are calculated following the strict definition related to the flow losses. The work was performed by Wang under supervision of Mihaescu and Fuchs. The paper was written by Wang and revised by Semlitsch, Mihaescu, and Fuchs. The manuscript is to be submitted for journal publication.

Paper 5

Assessing Energy Losses associated with the pulsating flow in the Exhaust Port of an Internal Combustion Engine.
Y. Wang & B. Semlitsch & M. Mihaescu & L. Fuchs .
Manuscript to be submitted for journal publication.

The purpose of this paper is to characterize the flow structures with flow decomposition methods. Proper Orthogonal Decomposition (POD) is used to analyze the coherent structures induced with the particular inflow and outflow conditions. The LES calculations were performed by Wang under supervision by Mihaescu and Fuchs. The post-processing of the LES data was completed by Wang and Semlitsch together, with Semlitsch taking care of the POD analysis of the data. The manuscript was revised by Mihaescu and Fuchs and it will be submitted for journal publication.

Acknowledgments

I would like to express my sincere gratitude to all the people who have guided, supported and helped me during the doctoral studies. Thank you for making this journey possible and enjoyable.

First of all, I am extremely grateful to my supervisor Professor Laszlo Fuchs, for your generous willingness and patience to share your vest knowledge and understanding in fluid mechanics and research. Your questions and comments are in keeping me on track. I believe that I will also benefit from these experiences in the future.

I express my special thanks to my co-supervisor Docent Mihai Mihaescu. Your enthusiasm, broad knowledge and perspectives are highly appreciated. I also really thank you for your kindly encouragement and valuable help during the research process.

Many thanks to Bernhard Semlitsch. I would like to say it is really happy to work with you.Thank you for your great ideas and help of my paper writing.

Thanks to Docent Anders Dahlkild, you gave me the first course in KTH and quite inspired me by the work. Professor Henrik Alfredsson, I have learned a lot from you about compressible flow. Thank you for providing me this important knowledge foundation of my study.

Thank you Johan Fjällman and Alexander Nygård for your support of Swedish translation.

Thank you Olle Bodin, especially for your sharing and help at the beginning of the project.

Great thanks to the colleagues at the department of mechanics and all the friends. Thank you for being with me through so many happy and unforgettable times. You know who you are!

I would also like to appreciate China Scholarship Council (CSC), for the finical support during my doctoral study. Thanks to Competence Center for

Gas Exchange (CCGEX), for great support of the project. PDC, NSC, LUNARC and HPC2N are acknowledged for the allocations of computational resources. Furthermore, I would like to thank my opponent and committee for participating in my journey to my PhD.

I am particularly grateful to my family. My parents and parents-in-law, who always give me warm care, encouragement and strong support during my studies.

Finally, most of all, I give my most heartfelt gratitude to my forever loved wife Juan Ren. Thank you for the endless love, understanding and support. Meeting you is the most wonderful miracle in my life!

感谢我的父亲、母亲；岳父、岳母以及所有亲朋好友对我的关心与支持！

谨以此献给我挚爱的妻子任娟，感谢她的付出与陪伴！

Bibliography

Adomeit, P., Lang, O., Pischinger, S., Aymanns, R., Graf, M. & Stapf, G. 2007 Analysis of cyclic fluctuations of charge motion and mixture formation in a DISI engine in stratified operation. In *SAE Technical Paper 2007-01-1412*.

Aghaali, H. & Angstrom, H. 2013 Demonstration of Air-Fuel Ratio Role in One-Stage Turbocompound Diesel Engines. In *SAE Technical Paper 2013-01-2703*.

Akselvoll, K. & Moin, P. 1993 Large Eddy Simulation of a Backward Facing Step Flow. *Engineering Turbulence Modeling and Experiments 2* **2**, 303–313.

Anderson, J. D. 1995 *Computational Fluid Dynamics: The Basics with Applications*. McGraw-Hill.

Armero, F. & Love, E. 2003 An arbitrary Lagrangian-Eulerian finite element method for finite strain plasticity. *Int. J. Numer. Methods Eng.* **57** (4), 471–508.

Baines, N. C. 2005 *Fundamentals of Turbocharging*. Vermont USA: Concepts NREC.

Baratta, M., Spessa, E. & Mairone, P. 2010 Numerical investigation of Turbolag reduction in HD CNG engines by means of exhaust valve variable actuation and spark timing control. *Journal of Automotive Technology* **11** (3), 289–306.

Barton, I. E. 1998 Comparison of SIMPLE- and PISO- Type Algorithms for transient flows. *International Journal for Numerical Methods In Fluids* **26**, 1787–1806.

Baum, E., Peterson, B., , Surmann, C., Michaelis, D., B.Böhm & Dreizler, A. 2013*a* Investigation of the 3D flow field in an IC engine using tomographic PIV. *Proceedings of the Combustion Institute* **34**, 2903–2910.

Baum, E., Peterson, B., B.Böhm & Dreizler, A. 2013*b* On the Validation of LES Applied to Internal Combustion Engine Flows: Part 1: Comprehensive Experimental Database. *Flow Turbulence Combust* .

Bensler, H., Kapitza, L., Raposo, J. & Reisch, U. 2002 A New Experimental Method for Determining Port Generated Swirl Flow. In *SAE Technical Paper 2002-01-2846*.

Bücker, I., Karhoff, D. C., Klaas, M. & Schröder, W. 2012 Stereoscopic multi-plannar PIV measurements of in-cylinder tumbling flow. *Exp. Fluids* **53**, 1993–2009.

Buschbeck, M., Bittner, N., Halfmann, T. & Arndt, S. 2012 Dependence of combustion dynamics in a gasoline engine upon the in-cylinder flow field, determined by high-speed PIV. *Experiments in Fluids* **32** (3), 1–12.

CD-Adapco 2011*a* Starccm+ User Guide 6.06.017. In *Tech. Report*.

CD-Adapco 2011*b* Starcd User Guide 4.16. In *Tech. Report*.

Crnojevic, C., Decool, F. & Florent, P. 1999 Swirl measurements in a motor cylinder. *Experiments in Fluids* **26** (6), 542–548.

Danov, S. 1997 Identification of discharge coefficients for flow through valves and ports of internal combustion engines. In *SAE Technical Paper 970642*.

Darwish, M. S. & Moukalled, F. 1994 Normalized Variable and Space Formulation Methodology for High-Resolution Schemes. *Num. Heat Trans., Part B* **26**, 79–107.

Dean, W. R. 1928 The streamline motion of fluid in a curved pipe. *Philosophical Magazine Series 7.* **5**, 673–695.

Decker, J. 2013 Critical and steady flow analysis of a high performance automotive exhaust port. PhD thesis, University of Miami, Coral Gables, Florida, USA.

Donea, J., Huerta, A., Ponthot, J.-P. & Rodrguez-Ferran, A. 2004 *Arbitrary LagrangianEulerian Methods. Encyclopedia of Computational Mechanics*. John Wiley & Sons, Ltd.

Ehrlich, D., Lawless, P. & Fleeter, S. 1997 On-Engine Turbocharger Turbine Inlet Flow Characterization. In *SAE Technical Paper*.

Electra, X. 2010 Supercharger vs. turbocharger. Technical report. See also URL `http://www.gearheadhaven.com/?p=1725`.

Fredrik, W., Christel, E. & ngström Hans-Erik, A. 2003 Correlation between engine simulations and measured data: experiences gained with 1D-simulations of turbocharged SI-engines. In *SIA International Congress*.

Fu, J., Liu, J., Yang, Y., Ren, C. & Zhu, G. 2013 A new approach for exhaust energy recovery of internal combustion engine: Steam turbocharging. *Applied Thermal Engineering* **52**, 150–159.

Galindo, J., Serrano, J., Climent, H. & Tiseira, A. 2008 Experiments and modeling of surge in small centrifugal compressor for automotive engines. *Experimental Thermal and Fluid Science* **32** (3), 818–826.

GammaTechnologiesInc. 2012 Flow Theory Manual. In *Tech. Report*.

Garmann, D. J., Visbal, M. R. & Orkwis, P. D. 2013 Comparative Study of implicit and Subgrid-Scale Model LES Techniques for Low-Reynolds Number Airfoil Applications. *International Journal for Numerical Methods in Fluids* **71** (12), 1546–1565.

Han, Z. & Reitz, R. D. 1995 Turbulence modeling of internal combustion engines using RNG $k - \epsilon$ models. *Combustion science and technology* **106**, 267–295.

Haworth, D. 1999 Large Eddy Simulation of In-cylinder Flow . *Oil Gas Sci. Technol.* **54** (2), 175–185.

Haworth, D. & Jansen, K. 2000 Large Eddy Simulation on Unstructured Deforming Mechs: Towards Reciprocating IC Engines . *Comput. Fluids* **29** (5), 493–524.

Hellström, F., Gutmark, E. & Fuchs, L. 2012 Large Eddy Simulation of the

Unsteady Flow in a Radial Compressor Operating Near Surge. *ASME Journal of Turbomach.* **53**, 1701–1712.

Heywood, J. B. 1988 *Internal Combustion Engine Fundamentals*. New York: McGraw-Hill Series in Mechanical Engineering.

Idelchik, I. E. 1986 *Handbook of Hydraulic Resistance*. New York USA: Harper & Row.

Ismail, A. R., Bakar, R. A. & Semin 2008 An Investigation of Valve Lift Effect on Air Flow and Coefficient of Discharge of Four Stroke Engines Based on Experiment. *American Journal of Applied Sciences* **5** (8), 963–971.

Joelsson, T., Yu, R., Bai, X. S., Vressner, A. & Johansso, B. 2008 Large eddy simulation and experiments of the auto-ignition process of lean ethanol/air mixture in HCCI engines. In *SAE Paper 2008-01-1668*.

Johansson, A. & Wallin, S. 2012 *Turbulence Lecture notes*. Stockholm Sweden: KTH.

Johanston, D., Edge, K. & Vaughan, N. 1991 Experimental Investigation of Flow and Force Characteristics of Hydraulic Poppet and Disc Valves. *Journal of Power and Energy* **205**, 161–171.

Kalpakli, A., Örlu, R. & Alfredsson, P. H. 2012 Dean vortices in turbulent flows: rocking or rolling? *Journal of Visualization* **15**, 37–38.

Kim, J., Moin, P. & Moser, R. 1987 Turbulence statistics in fully developed channel flow at low Reynolds number. *J. Fluid Mech.* **177**, 133–166.

Kitto, J. B. & Stultz, S. C. 1978 *Steam: Its Generation and Use*. The Babcock & Wilcox Company.

Kumar, C. R. & Nagarajan, G. 2012 Investigation of Flow During Intake Stroke of a Single Cylinder Internal Combustion Engine. *ARPN Journal of Engineering and Applied Sciences* **7** (2), 180–186.

Kundu, P. K., Cohen, I. M. & Dowling, D. R. 2012 *Fluid Mechanics*. Elsevier Inc.

Kurniawan, W. H., Abdullah, S. & Shamsudeen, A. 2007 Turbulence and Heat Transfer Analysis of Intake and Compression Stroke in Automotive 4-stroke Direct Injection Engine. *Algerian Journal of Applied Fluid Mechanics* **1**, 37–50.

Lee, H., Moin, P. & Kim, J. 1997 Direct Numerical Simulation of Turbulent Flow over a Backward-Facing Step. *Journal of Fluid Mechanics* **330**, 349–374.

Leer, B. V. 1977 Towards the ultimate conservative difference scheme. *Journal of Computational Physics* **23**, 276–299.

Leonard, B. P. 1991 The ULTIMATE conservative difference scheme applied to unsteady one-dimensional advection. *Comp. Methods in Applied Mechanics and Engineering* **88**, 17–74.

Margolin, L. G., Rider, W. J. & Grinstein, F. F. 2006 Modeling turbulent flow with implicit LES. *Journal of Turbulence* **7**, 1–27.

Masi, M., Toffolo, A. & Antonello, M. 2010 Experimental Analysis of a Motorbike High Speed Racing Engine. *Applied Energy* **87**, 1461–1650.

Müller, S., Böhm, B., ner, M. G., Grzeszik, R., Arndt, S. & Dreizler, A.

2010 Stereoscopic multi-plannar PIV measurements of in-cylinder tumbling flow. *Exp. Fluids* **48**, 281–290.

Onorati, A., Cerri, T., Ceccarani, M. & Cacciatore, D. 2005 Experimental Analysis and 1D Thermo-Fluid Dynamic Simulation of a High Performance Lamborghini V10 S.I. Engine. In *SAE Technical Paper 2005-24-081*.

Onorati, A., Ferrari, G. & D'Errico, G. 2003 Secondary Air Injection in the Exhaust After-Treatment System of S.I. Engines: 1D Fluid Dynamics Modeling and Experimental Investigation. In *SAE Technical Paper 2003-01-0366*.

Onorati, A., Ferrari, G., D'Errico, G. & Montenegro, G. 2002 The prediction of 1D Unsteady Flows in the Exhaust System of a S.I. Engine Including Chemical Reactions in the Gas and Solid Phase. In *SAE Technical Paper 2002-01-0003*.

Peterson, B., Baum, E., B.Böhm, Sick, V. & Dreizler, A. 2013 High-speed PIV and LIF imaging of temperature stratification in an internal combustion engine. *Proceedings of the Combustion Institute* **34**, 3653–3660.

Piscaglia, F., Montorfano, A. & Onorati, A. 2013 Towards the LES Simulation of IC Engines with Parallel Topologically Changing Meshes. *SAE Int. J. Engines* **6**, 2013.

Piscaglia, F., Onorati, A., Marelli, S. & Capobianco, M. 2007 Unsteady Behavior in Turbocharger Turbines: Experimental Analysis and Numerical Simulation. In *SAE Technical Paper 2007-24-0081*.

Pope, S. B. 2000 *Turbulence Modeling for CFD*. Cambridge, UK: Cambridge university press.

Reynolds, O. 1883 An experimental investigation of the circumstances which determine whether the motion of water shall be direct or sinuous, and of the law of resistance in parallel channels. *Philosophical Transactions of the Royal Society* **174** (0), 935–982.

Rezaei, R., Pischinger, S., Ewald, J. & Adomeit, P. 2010 A new CFD approach for assessment of swirl flow pattern in HSDI diesel engines. In *SAE Technical Paper 2010-32-0037*.

Robert, L. M. 2005 *Applied Fluid Mechanics*. Oxford UK: Pearson Prentice Hall.

Rutland, C. J. 2011 Large eddy simulations for inter combustion engines - a review. *International Journal of Engine Research* **12**, 421–451.

Rutten, F., Schroder, W. & Meinke, M. 2005 Large-eddy simulation of lowfrequency oscillations of the Dean vortices in turbulent pipe bend flows. *Physics of Fluids* **17** (3), 035107.

Sarkar, S. & Balakrishnan, L. 1990 Application of a Reynolds-stress turbulence model to the compressible shear layer. In *ICASE Report*.

Shyy, W. 1994 *Computational modeling of fluid flow and interfacial transport*. Elsevier Science Publishers B. V.

Smagorinsky, J. 1963 General circulation experiments with the primitive equations: I. The basic equations. *Mon Weather Rev* **91**, 99–164.

Smits, J. 2006 Modeling of a Fluid Flow in an Internal Combustion Engine. In *Tech. Report*.

Tahry, E. & H., S. 1983 $k - \epsilon$ equation for compressible reciprocating engine flows. *Journal of Energy* **7**, 345–353.

Towers, D. & Towers, C. 2004 Cyclic variability measurements of in-cylinder engine flows using high-speed particle image velocimetry. *Meas. Sci. Tech.* **15**, 1917–1925.

Versteeg, H. K. & W.Malalasekera 1995 *An introduction to Computational Fluid Dynamics The Finite Volume Method*. London UK: Longman Scientific & Technical.

Wang, Y., Semlitsch, B., Mihaescu, M. & Fuchs, L. 2013 Flow structures and losses in the exhaust port of an Internal combustion engine. In *In the proceedings of the ASME 2013 International Mechanical Engineering Congress & Exposition*.

Watson, N. & Janota, M. S. 2005 *Turbocharging the Internal Combustion Engine*. London: London: The MacMillan Press Ltd.

Wilcox, D. C. 2006 *Turbulence Modeling for CFD*. California, USA: DCW Industries.

Yu, R., Bai, X. S., Hildingsson, L., Hultqvist, A. & Miles, P. 2006 Numerical and experimental investigation of turbulent flows in a Diesel engine. In *SAE Paper 2006-01-3436*.

Yu, R., Bai, X. S., Vressner, A., Hultqvist, A., Johansson, B., Olofsson, J., Seyfried, H., Sjoholm, J., Richter, M. & Alden, M. 2007 Effect of turbulence on HCCI combustion. In *SAE Paper 2007-01-0183*.

Zalesak, S. T. 1979 Fully multidimensional flux-corrected transport algorithms for fluids. *Journal of Computational Physics* **31**, 355–362.

Part II

Papers